How sphericity combines with the age and width of slabs to dictate the dynamics and evolution of subduction systems on Earth

Fangqin Chen[1], D. Rhodri Davies[1], Saskia Goes[2], Lior Suchoy[2], and Stephan C Kramer[2]

[1]Australian National University
[2]Imperial College London

November 21, 2022

Abstract

The role of Earth's spherical geometry in modulating the evolution of subduction zones is poorly understood. Here, we simulate multi-material free-subduction in a 3-D spherical shell domain, to investigate the effect of plate thickness, density (combined approximating age) and width on the evolution of subduction systems. To isolate the role of sphericity, we compare results with equivalent Cartesian models. The first-order predictions of our spherical cases are generally consistent with existing Cartesian studies: (i) slabs retreat more, at a shallower dip, as plate age increases, due to increased bending resistance and sinking rates; and (ii) wider slabs can develop along-strike variations in trench curvature, trending towards a 'W'-shape, due to toroidal flow at slab edges. We find, however, that these along-strike variations are restricted to older, stronger, retreating slabs. When compared to slabs in Cartesian models, in a spherical domain: (i) slabs descend faster, due to the convergence of downwelling material with depth; (ii) these faster sinking rates reduce the time available for bending at the trench, resulting in effectively stronger slabs; (iii) the curvature of slabs increases their effective strength; and (iv) the curvature of the transition zone tends to enhance slab stagnation. These differences between spherical and Cartesian cases become more prominent as slab width increases. Taken together, our results suggest that Cartesian models are suitable for simulating narrow subduction zones, but spherical models should be utilised when investigating subduction zones wider than ˜ 2000 km: at such length-scales, the consequences of Earth's curvature cannot be ignored.

How sphericity combines with the age and width of slabs to dictate the dynamics and evolution of subduction systems on Earth

Fangqin Chen[1], D. Rhodri Davies[1], Saskia Goes[2], Lior Suchoy[2], Stephan C. Kramer[2]

[1]Research School of Earth Sciences, The Australian National University, Canberra, ACT, Australia
[2]Department of Earth Science and Engineering, Imperial College London, London, UK

Key Points:

- The dynamics of subduction systems depend on the thickness, density (combined approximating age) and width of the downgoing plate.
- Subducting slabs in a spherical geometry exhibit a greater effective strength than equivalent slabs in a Cartesian geometry.
- The effect of Earth's curvature becomes significant when simulating subduction systems wider than $\sim 2000\,\mathrm{km}$.

Corresponding author: Fangqin Chen, `Fangqin.Chen@anu.edu.au`

Abstract
The role of Earth's spherical geometry in modulating the evolution of subduction zones is poorly understood. Here, we simulate multi-material free-subduction in a 3-D spherical shell domain, to investigate the effect of plate thickness, density (combined approximating age) and width on the evolution of subduction systems. To isolate the role of sphericity, we compare results with equivalent Cartesian models. The first-order predictions of our spherical cases are generally consistent with existing Cartesian studies: (i) slabs retreat more, at a shallower dip, as plate age increases, due to increased bending resistance and sinking rates; and (ii) wider slabs can develop along-strike variations in trench curvature, trending towards a 'W'-shape, due to toroidal flow at slab edges. We find, however, that these along-strike variations are restricted to older, stronger, retreating slabs. When compared to slabs in Cartesian models, in a spherical domain: (i) slabs descend faster, due to the convergence of downwelling material with depth; (ii) these faster sinking rates reduce the time available for bending at the trench, resulting in effectively stronger slabs; (iii) the curvature of slabs increases their effective strength; and (iv) the curvature of the transition zone tends to enhance slab stagnation. These differences between spherical and Cartesian cases become more prominent as slab width increases. Taken together, our results suggest that Cartesian models are suitable for simulating narrow subduction zones, but spherical models should be utilised when investigating subduction zones wider than ~ 2000 km: at such length-scales, the consequences of Earth's curvature cannot be ignored.

Plain Language Summary

Subduction zones are locations where Earth's tectonic plates collide, and the denser plate subsequently descends into the mantle. They exert important controls on surface plate motions and plate boundary deformation, and help to organise underlying mantle flow. As a result, this important process has been extensively studied through both analogue and computational models. However, most of these models have been undertaken in a rectangular box instead of in an Earth-like sphere. Here, we model the dynamics and evolution of subduction systems on a sphere, and find that although our results are similar to the general findings that have been made with box models, there are important differences between these two setups. The curved shape of tectonic plates on a sphere makes them effectively stronger than in the box models and this affects their velocities and shape. They also sink faster in the spherical domain. We find that while box models are suitable for studying narrow plates, we need to model in a spherical setting to study wider subduction zones. Using this spherical setup, we show how the age and width of a subducting plate combine to dictate the evolution of subduction zones on Earth.

1 Introduction

During subduction, the oceanic lithosphere of one tectonic plate dives beneath another at a convergent margin and is recycled into Earth's mantle (e.g., Stern, 2002; Kearey et al., 2009). As subducted slabs descend, their negative buoyancy provides a key driving force for plate tectonics, and they continue to influence surface processes in a number of ways (e.g., Forsyth & Uyeda, 1975; Lithgow-Bertelloni & Richards, 1998; Wheeler & White, 2002). Seismic images of Earth's interior reveal that when slabs descend towards the mantle transition zone, at depths of 410–660 km that coincide with several mineralogical phase transformations and a likely viscosity increase, some stall and are horizontally deflected (e.g., the Ryuku, Izu-Bonin and Honshu slabs), some thicken and buckle (e.g., the Marianas slab), whilst others appear to pass through unhindered (e.g., the Cocos and Antilles slabs): their imaged morphologies are far from uniform (e.g., Karato et al., 2001; Li et al., 2008; Goes et al., 2017; van der Meer et al., 2018). The dominant controls on such variations remain unclear, and likely vary between different subduction zones, due to complexities arising from non-linear and multi-scale interactions between several aspects of the mantle system, including downgoing and overriding plate properties, global mantle flow, mineral phase changes and material rheology (e.g., Karato et al., 2001; Čížková et al., 2002; Capitanio et al., 2007; Schellart et al., 2007; Goes et al., 2008; Stegman, Farrington, et al., 2010; Garel et al., 2014; Goes et al., 2017; Agrusta et al., 2017).

The observational record does not support a clear correlation between slab morphology and subducting plate age (e.g., Lallemand et al., 2005; Sdrolias & Müller, 2006; Goes et al., 2011), implying that variations in a slab's age along the trench, trench width, local sources of buoyancy such as oceanic plateaus and aseismic ridges, complexities associated with overriding plates and regional tectonics, can all affect the evolution of subducting slab morphology. Several studies have investigated the factors controlling the evolution of subducted slabs, mostly in either 2-D or 3-D Cartesian domains, in an attempt to reconcile predictions from geodynamical modelling with the observed morphologies (e.g., Čížková et al., 2007; Schellart et al., 2007; Capitanio et al., 2010; Mason et al., 2010; Stegman, Farrington, et al., 2010; Sharples et al., 2014; Garel et al., 2014; Holt et al., 2015).

The age of a subducting slab determines its thermal structure, which controls slab thickness, density and rheology. In turn, these control slab strength and buoyancy, which combine to determine the rate of trench retreat (e.g., Bellahsen et al., 2005; Capitanio et al., 2007; Di Giuseppe et al., 2008; Schellart, 2008; Ribe, 2010; Stegman, Farrington, et al., 2010; Garel et al., 2014; Goes et al., 2017). It is well-established that trench-motion history correlates with slab morphology (e.g., van der Hilst & Seno, 1993; Faccenna et al., 2001; Goes et al., 2017). Goes et al. (2008) suggest that older, colder, oceanic lithosphere is stronger due to the temperature dependence of viscosity, and that this drives significant trench retreat, with slabs more likely to lie flat at the mantle transition zone; conversely, younger lithosphere is weaker and subducts with less trench retreat, tending to buckle at the mantle transition zone. This direct link between slab age and the style of slab-transition zone interaction is supported by laboratory and numerical simulations (e.g., Schellart, 2004; Bellahsen et al., 2005; Capitanio et al., 2007; Funiciello et al., 2008; Garel et al., 2014; Goes et al., 2017).

Slab width also plays an important role in determining the evolution of subduction zones, affecting the shape and curvature of the trench, through an influence on the rate of trench retreat (e.g., Stegman et al., 2006; Schellart et al., 2007; Stegman, Schellart, & Freeman, 2010; Strak & Schellart, 2016). Schellart et al. (2007) advocate an inversely proportional relationship between trench migration rates and the width of subduction zones. In their models, wider slabs develop upper mantle stagnation zones, where the centre of the trench exhibits negligible trench retreat compared to the edges of the trench. Such a relationship is observed in large subduction systems such as the South American subduction zone, and could be responsible for the varying styles of slab morphology along wide trenches.

Plate interactions and lateral variations in plate properties also influence the geometry and evolution of subducting plates. The structure and motion of overriding plates have an effect on slab dip, trench migration, and slab interaction with the mantle transition zone (e.g., Jarrard, 1986; Lallemand et al., 2005; Heuret et al., 2007; Capitanio et al., 2010; van Dinther et al., 2010; Garel et al., 2014). The subduction of locally thickened oceanic lithosphere, such as oceanic plateaus, aseismic ridges or seamount chains has been proposed to influence the shape of the trench and change the geometry of subducting slabs (e.g., Cross & Pilger, 1982; Gutscher, Malavieille, et al., 1999; Martinod et al., 2005; Capitanio et al., 2011). The higher compositional buoyancy of oceanic plateaus and ridges could resist slab sinking into the mantle and, thus, potentially lead to flat slab subduction (e.g., van Hunen et al., 2002; Mason et al., 2010). These factors add to the complexity of observed slab morphology, and may explain why no simple correlations to plate properties can be made to explain slab morphology.

Existing numerical and laboratory studies in an enclosed Cartesian domain provide valuable insight into the sensitivity of slab morphology to a number of controlling parameters. However, Earth's mantle is a spherical shell, where gravity points radially towards the center and is bounded only by Earth's surface and the core-mantle boundary at $\sim$ 2890 km depth: there are no side boundaries. In addition, the mantle closes in upon itself under geometrical and gravitational constraints, requiring 10% shortening in any lateral direction when a slab descends from Earth's surface to the transition zone. Earth's surface is also curved in two orthogonal directions and this 'double curvature' likely increases the geometric stiffness of slabs (e.g. Mahadevan et al., 2010). As a consequence, the applicability of Cartesian simulations for investigating the evolution of subduction systems on Earth remains unclear, particularly for wider subduction zones.

Very few studies have investigated the role of Earth's spherical geometry in controlling the dynamical evolution of subduction systems. To our knowledge, Morra et al. (2009) were the first to use spherical models at the planetary scale to demonstrate that during subduction, Earth's curvature can drive the development of concave curvatures at plate edges and, for wider plates, complex folding at the centre that becomes more pronounced at depth. Morra et al. (2012) incorporated a viscosity jump at 660 km depth, and demonstrate that slab-transition-zone interaction can drive lateral heterogeneity in trench behaviour. The Boundary Element Method (BEM) used in these studies (e.g., Pozrikidis, 1992; Morra et al., 2007) has also been applied to examine the influence of overriding plates on subduction (Butterworth et al., 2012), and intra-plate deformation of the Pacific plate in the early Cenozoic (Butterworth et al., 2014). The BEM approach has many advantages over traditional finite element approaches, including increased numerical efficiency. However, there are also important limitations, including difficulties in simulating anything but isoviscous plates. This is a major shortcoming as a growing body of (Cartesian) studies demonstrate that complex plate rheology is fundamental to reproducing the dynamics of subduction on Earth (e.g., OzBench et al., 2008; Capitanio et al., 2010; Stegman, Farrington, et al., 2010; Garel et al., 2014; Király et al., 2017).

In this paper, we build on the insights gained from these previous Cartesian studies, to examine the role of Earth's sphericity in controlling subduction dynamics in simulations that incorporate a composite visco-plastic plate rheology. Our aim is to investigate the effect of subducting plate age and width on slab morphology using 3-D spherical numerical models of free subduction, and to isolate the role of sphericity by comparing results to Cartesian simulations. We use Fluidity (e.g., Davies et al., 2011; Kramer et al., 2012; Davies et al., 2016; Kramer et al., 2021), an anisotropic, adaptive, unstructured mesh computational modelling framework, to examine comparable cases, for a range of slab densities, thicknesses and widths, in both Cartesian and spherical geometries. We aim to identify the critical threshold beyond which Cartesian models are no longer appropriate for examining subduction systems on Earth, and the sensitivity of this threshold to plate properties. We examine three combinations of plate thickness and density to estimate the effect of different plate ages ranging from young ($\sim$ 10 Myr, estimated using a half space cooling model) to old ($\sim$ 140 Myr), noting that the range of subducting plate ages on Earth is 0 - 160 Myr (e.g. Müller et al., 2016). Motivated by a compilation of global trench lengths at the present-day (Heuret et al., 2011) and Cenozoic Era reconstructions (Müller et al., 2016), we examine trench widths of 1200, 2400, 3600 and 4800 km. As illustrated in Figure 1, at the present-day, most trenches are less than 5000 km wide, with mean and median widths of 1940 km and 1130 km for the dataset of Heuret et al. (2011) and 2000 km and 1230 km for the dataset of Müller et al. (2016). At 60 Ma (where there are less data on narrow trenches), mean and median widths are 3520 km and 3430 km (Müller et al., 2016). It is noteworthy that very few trenches exceed 6000 km in width: at present, the South America trench is 7060 km wide, and the Sumatra-Andaman-

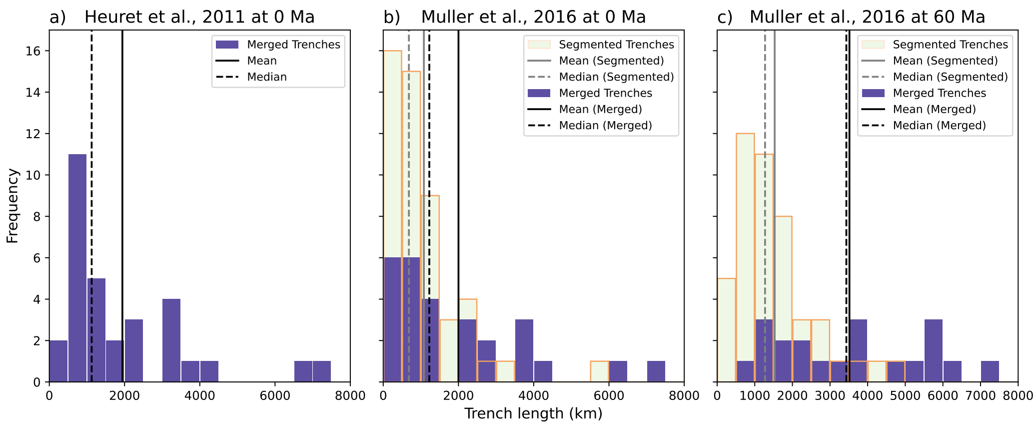

Figure 1. (a) Present-day trench length histogram compiled from rupture segment lengths by Heuret et al. (2011) and combined here for commonly recognised continuous trenches (see Supplementary Information Figure S1); (b) and (c) trench length histograms based on global tectonic plate reconstructions, at the present-day and at 60 Ma respectively Müller et al. (2016). The reconstructed trenches are segmented based on changes in lower or upper plate characteristics (green bars with orange outline). Based on lower plate properties, we merged segments that likely subduct as coherent slabs (purple bars). Note that corresponding maps of trench segments are provided in Figure S1.

Java-Timor trench exceeds 6040 km width; at 60 Myr, the South America and Aleutian trenches were $\sim$ 7100 and $\sim$ 6070 km wide, respectively (Müller et al., 2016). Global maps of the trenches included in the compilations of Figure 1 are provided in Supplementary Figure S1.

The paper is structured as follows. We first describe the governing equations, material properties, initial and boundary conditions and other aspects of our numerical model setup, in addition to listing the different cases examined. We subsequently present a systematic quantitative comparison between simulations in Cartesian and spherical domains, to demonstrate: (i) how slab thickness and density (approximating slab age) and slab width affects the evolution of subducting slabs; and (ii) the significance of Earth's sphericity in modulating subduction dynamics. We end by discussing our results and their implications for an improved understanding of subduction on Earth.

2 Model Description

2.1 Governing Equations and Numerical Strategy

We simulate multi-material free-subduction of a composite visco-plastic plate into an ambient mantle, in both 3-D Cartesian and 3-D hemispherical shell domains, which extend from the surface to a depth of 2890 km. Assuming incompressibility, the governing equations for this problem are the continuity equation,

$$\nabla \cdot u = 0 \tag{1}$$

the Stokes equation,

$$-\vec{\nabla} p + \nabla \cdot \left[\mu \left(\vec{\nabla} u + \left(\vec{\nabla} u \right)^T \right) \right] = g \Delta\rho \Gamma \hat{k} \tag{2}$$

and an advection equation for composition,

$$\frac{\partial \Gamma}{\partial t} + \mathbf{u} \cdot \vec{\nabla} \Gamma = 0 \tag{3}$$

where u is velocity, p the pressure, μ the viscosity, ρ the density, g gravity acceleration, $\hat{k}$ unit vector in the direction opposite gravity, and Γ the material volume fraction ($\Gamma = 1$ in a region occupied by a given material and $\Gamma = 0$ elsewhere).

Simulations are carried out using Fluidity (e.g., Davies et al., 2011; Kramer et al., 2012), a computational modelling framework supporting finite element and control volume discretisations, which has recently been validated in a spherical shell domain against an extensive set of analytical solutions introduced by Kramer et al. (2021). In the context of this study, the framework has several ideal features. Fluidity: (i) can run in 2-D and 3-D, Cartesian and spherical domains; (ii) uses an unstructured mesh, which enables the straightforward representation of complex geometries and materials; (iii) dynamically optimizes this mesh, across parallel processors, providing increased resolution in areas of dynamic importance, thus allowing for accurate simulations across a range of length-scales, within a single model; (iv) enhances mesh optimization using anisotropic elements; (v) can employ a free-surface boundary condition, which is important for correctly capturing slab decoupling from the surface (Kramer et al., 2012); (vi) utilises the highly-scalable parallel linear system solvers available in PETSc (Balay et al., 1997), which can efficiently handle sharp, orders of magnitude variations in viscosity; and (vii) has a novel interface-preservation scheme, which conserves material volume fractions and allows for the incorporation of distinct materials (Wilson, 2009). In this study, Fluidity's adaptive mesh capabilities are utilised to provide a local resolution of 3 km in regions of dynamic significance (i.e. at the interface between materials and in regions of strong velocity and viscosity contrasts), with a coarser resolution of up to 300 km elsewhere. It is this adaptive mesh functionality that makes our global spherical simulations computationally tractable.

2.2 Geometry, Boundary Conditions and Material Properties

The configuration of our models are inspired by Stegman, Farrington, et al. (2010) and Garel et al. (2014). Both Cartesian and spherical simulations utilise the symmetry of the model to halve the computational domain's extent.

For Cartesian simulations (Figure 2a), the domain is 4000 km long, 2890 km deep, whilst the width (W) depends on the width of the plate (w) where $w/W = 0.3$. When non-dimensionalised with characteristic depth $H = 2890$ km, the domain depth becomes 1. The Cartesian model has a free-surface, with free-slip conditions elsewhere, including the symmetric mid-plane. The gravity direction is vertical. For spherical simulations (Figure 2b), the domain is a hemispherical shell with outer and inner radii that correspond to Earth's surface and core-mantle-boundary (CMB), respectively (Figure 2). When non-dimensionalised, the hemispherical shell has an outer radius of 2.22 and an inner radius 1.22, thus the computational domain has thickness of 1, and is equivalent to its Cartesian counterpart. The spherical model has a free-surface boundary condition on the outer surface, with a free-slip condition on the symmetry plane and CMB. The gravity direction points radially towards the centre of the sphere.

The subducting plate length (L) is 2200 km. In Cartesian models, the tail of the plate is 600 km from the edge of the domain. The initial slab tip geometry is prescribed with a bending radius of 250 km and an angle of 77° (Figure 2c). The subducting lithosphere is a composite plate comprising a core isoviscous layer embedded in upper and lower visco-plastic layers with viscosities following a von Mises law, building on OzBench et al. (2008). Upper and lower plates are assigned the minimum viscosity between the Newtonian viscosity μ_{Newt} and an effective von Mises viscosity μ_{vM}, such that purely viscous deformation occurs as long as the second invariant of the stress tensor $\tau_{II} = 2\mu\dot{\varepsilon}_{II}$

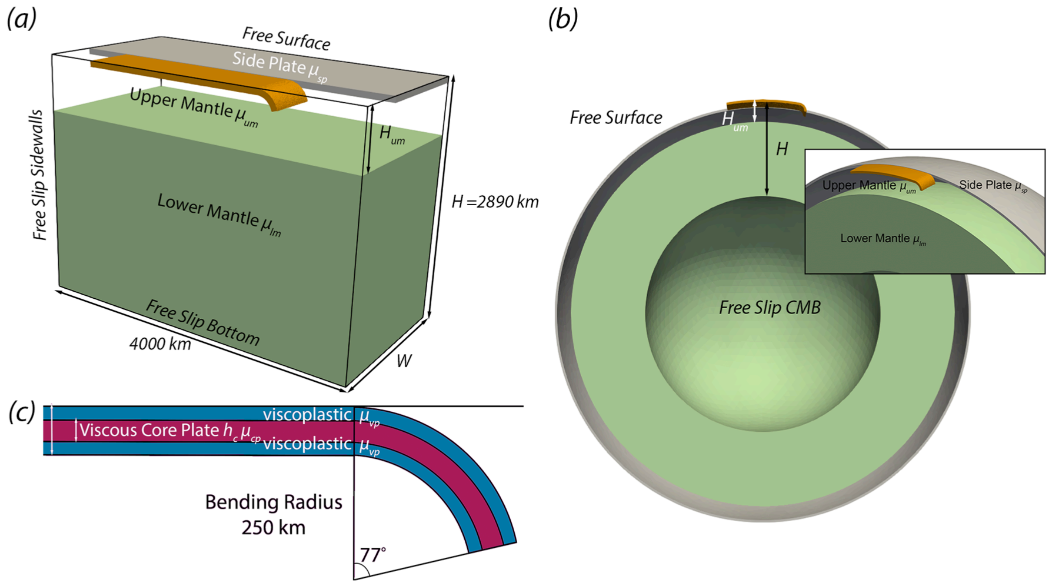

Figure 2. Setup of our simulations in: (a) a Cartesian geometry; and (b) a spherical geometry. In both geometries, we exploit the symmetry of the system, allowing us to halve the computational domain's extent, whilst bottom and top (inner and outer) boundaries approximate Earth's core-mantle-boundary and surface, respectively. (c) Initial slab tip geometry of our layered visco-plastic plates.

(where $\dot{\varepsilon}_{II}$ is the second invariant of strain rate tensor) does not reach the critical yield stress, τ_{yield}. The effective viscosity of visco-plastic layers is given by:

$$\mu_{\text{vM}} = \begin{cases} \frac{\tau_{II}}{2\dot{\varepsilon}_{II}}, & \text{if } \tau < \tau_{\text{yield}} \\ \frac{\tau_{\text{yield}}}{2\dot{\varepsilon}_{II}}, & \text{if } \tau \geq \tau_{\text{yield}} \end{cases} \tag{4}$$

At material interfaces, the average viscosity is calculated through a geometric mean,

$$\mu_{\text{ave}} = \mu_1^{\Gamma_1} * \mu_2^{\Gamma_2}, \tag{5}$$

where μ_i is the viscosity of material i, and Γ_i is the relative volume fraction of material i in the vicinity of the finite-element node at which the effective viscosity μ_{ave} is needed.

A side plate covers the entire domain adjacent to the subducting plate. It has the same thickness as the plate, and is placed 22 km away from the plate's edge. It is 1000 times more viscous than adjacent upper mantle material, and is required to prevent lateral flow narrowing the width of downgoing plate (as in Holt et al., 2017). The lower mantle is 50 times more viscous than the upper mantle, with the viscosity jump occurring at 660 km depth. Model parameters common to all simulations are listed in Table 1.

2.3 Cases Examined and Quantitative Model Diagnostics

We investigate 9 cases, across a wide parameter-space, in both Cartesian and spherical coordinate systems, with an additional three spherical cases at a plate width of 3600 km, totalling 21 cases. We systematically varied plate thickness (h), core plate thickness(h_c), density contrast between plate and adjacent mantle ($\Delta\rho$) and plate width (w) to examine how these influence the evolution of subduction and slab morphologies. Our choices are motivated by subduction regime diagrams, as a function of plate age and width, from

Table 1. Parameters common to all simulations.

Parameter	Symbol	Value
Gravitational acceleration	g	$10\ \mathrm{m/s^2}$
Characteristic depth (whole mantle)	H	2890 km
Depth of upper mantle	H_{um}	660 km
Upper mantle reference viscosity	μ_{um}	2.0×10^{20} Pa s
Lower mantle reference viscosity	μ_{lm}	$50 \times \mu_{um}$
Core plate viscosity	μ_{cp}	$100 \times \mu_{um}$
Initial viscosity of visco-plastic layer	μ_{Newt}	$100 \times \mu_{um}$
Side plate viscosity	μ_{sp}	$1000 \times \mu_{um}$
Mantle density	ρ	$3300\ \mathrm{kg/m^3}$
Yield stress	τ_{yield}	100 MPa

Table 2. Simulations examined and associated model parameters.

Case	h (km)	h_c (km)	$\Delta\rho$ (kg m^{-3})	w (km)	Domain Type
W1200_young	45	15	40	1200	Cartesian & Spherical
W1200_ref	70	30	80	1200	Cartesian & Spherical
W1200_old	100	40	120	1200	Cartesian & Spherical
W2400_young	45	15	40	2400	Cartesian & Spherical
W2400_ref	70	30	80	2400	Cartesian & Spherical
W2400_old	100	40	120	2400	Cartesian & Spherical
W4800_young	45	15	40	4800	Cartesian & Spherical
W4800_ref	70	30	80	4800	Cartesian & Spherical
W4800_old	100	40	120	4800	Cartesian & Spherical
W3600_young	45	15	40	3600	Spherical
W3600_ref	70	30	80	3600	Spherical
W3600_old	100	40	120	3600	Spherical

other studies (e.g., Stegman, Schellart, & Freeman, 2010; Garel et al., 2014; Goes et al., 2017). The combinations of plate thickness and density contrast produce a range of subduction behaviour from a vertical-folding type young plate to a retreating and flattening old plate. In the following sections, the plate widths refer to the full widths of the plate. In practice, we only simulate half of the width exploiting the symmetry of the domain. When combined, these cases allow us to compare the effect of plate age, which influences the thickness and density contrast of a slab, and plate width, on the evolution of subduction. Case names, alongside their key parameter values, are listed in Table 2.

To quantify how these parameters influence results, we have calculated several diagnostic outputs from these cases. When doing so, the boundary of the slab is defined as the 0.5 contour of the mantle material volume fraction (material volume fraction = 1 when the material is mantle, 0 otherwise). Based on this contour, we extract the slab tip depth, the trench location and the trailing edge position, as well as rates of slab descent, trench retreat and plate advance. We calculate the average slab dip in the upper mantle from the surface to 650 km depth, with respect to the direction of gravity at the slab centre at 325 km depth. In Cartesian domains, the direction of gravity is always vertical, whereas for spherical models, the direction of gravity is radially towards the centre of the sphere from the point of measurement. The measurements are taken at the symmetry plane unless otherwise specified. We also trace the evolution of trench geometry relative to the initial trench shape.

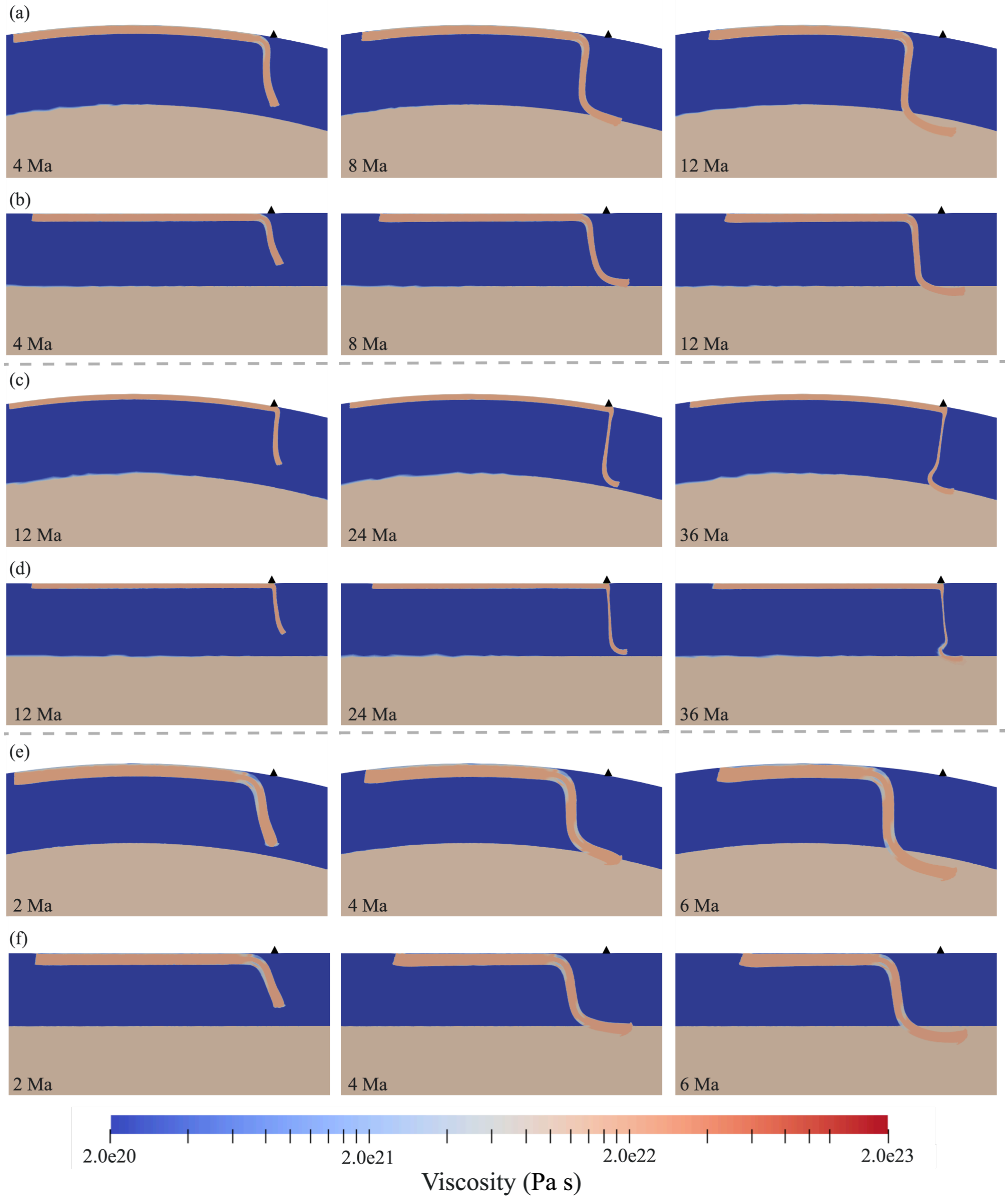

Figure 3. Snapshots illustrating the spatio-temporal evolution of slab morphology through the viscosity field, for spherical and Cartesian models with a plate width of 1200 km: (a) spherical; and (b) Cartesian cases, with $H = 70\,\mathrm{km}$ and $\Delta\rho = 80\,\mathrm{kg\,m^{-3}}$; (c) spherical and (d) Cartesian models with $H = 45\,\mathrm{km}$ and $\Delta\rho = 40\,\mathrm{kg\,m^{-3}}$; (e) spherical and (f) Cartesian models with $H = 100\,\mathrm{km}$ and $\Delta\rho = 120\,\mathrm{kg\,m^{-3}}$.

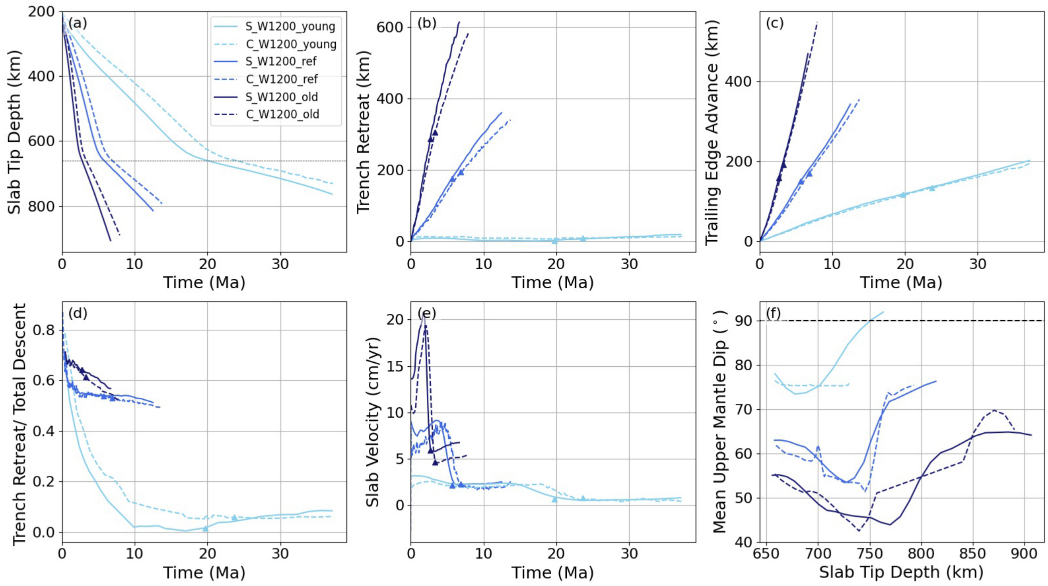

Figure 4. Comparison between spherical and Cartesian simulations with a plate width of 1200 km: (a) slab tip depth, as a function of time, where the upper–lower mantle boundary is indicated by the black dotted line at 660 km depth; (b) amount of trench retreat; (c) amount of plate advance, measured at the plate's trailing edge; (d) ratio of trench retreat to total descent, which is the sum of trench retreat and trailing edge advance; (e) slab sinking velocity; and (f) average slab dip in the upper mantle, with the black dashed line indicating a vertical slab with dip angle of 90°. Triangles indicate the time of slab tip transition-zone interaction. All measurements are taken at the symmetry plane.

3 Results

3.1 Reference Case

Case W1200_ref is selected as our reference, given its mid-range plate density and thickness, and width that sits towards the lower end of trench lengths on Earth. The temporal evolution of this case, in both spherical and Cartesian domains, is illustrated in Figure 3(a,b), and both yield similar slab morphologies. As subduction initiates, the slab tip steepens. During the upper mantle sinking phase (Figure 4a), the trench steadily retreats from its initial position (Figure 4b) with ∼50% of subduction accommodated via this trench retreat (over 60% in the early stages), despite the trailing edge of the plate advancing steadily (Figure 4c,d). As the trench retreats, it develops a concave 'C' shape, as illustrated in Figure 5(b). Following interaction with the viscosity jump at 660 km depth, the slab tip is deflected, the slab sinking rate reduces substantially (Figure 4a,e), and the upper mantle section of the slab steepens (Figure 4f). The slab then slowly sinks into the lower mantle.

Coupling of the sinking plate with adjacent mantle drives toroidal and poloidal mantle flow (e.g., Schellart, 2004; Funiciello et al., 2006; Stegman et al., 2006). Figure 6(a-c) illustrates tangential flow at 300 km depth for the spherical case at different stages of subduction: the toroidal cell around the edge of the plate drives the increasing concavity of the trench (Figure 5b). Figure 6(d-f) shows vertical cross-sections through the symmetry plane: two poloidal cells can be identified as the slab sinks in the upper mantle, one above the downgoing plate in the mantle wedge, and the other in the sub-slab re-

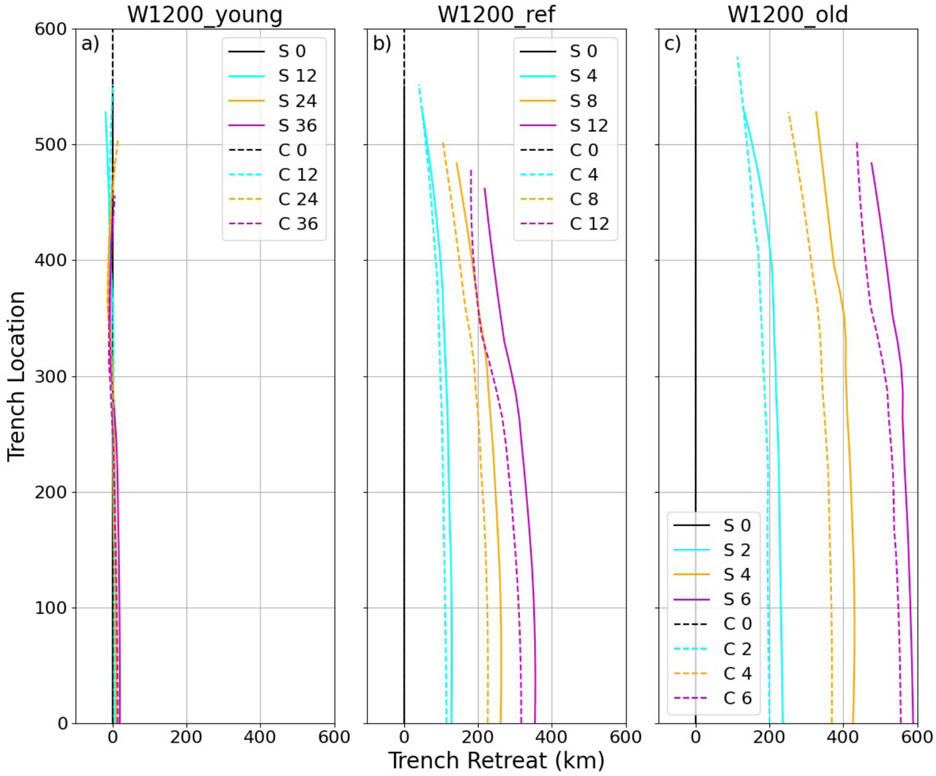

Figure 5. Spatio-temporal evolution of trench location in spherical (S, solid) and Cartesian (C, dashed) simulations, at a plate width of 1200 km. Times given in Myr since simulation initiation. (a) $H = 45\,\mathrm{km}$, $\Delta\rho = 40\,\mathrm{kg\,m^{-3}}$; (b) $H = 70\,\mathrm{km}$, $\Delta\rho = 80\,\mathrm{kg\,m^{-3}}$; (c) $H = 100\,\mathrm{km}$, $\Delta\rho = 120\,\mathrm{kg\,m^{-3}}$.

gion. During the upper-mantle phase of subduction, the mantle wedge cell is more prominent, while flow velocities in this cell diminish as the slab tip deflects and sinks into the more viscous lower mantle.

Cartesian and spherical models generally evolve in a similar manner in space and time. However, there are subtle differences that persist across all cases examined: (i) spherical models exhibit faster sinking rates than their Cartesian counterparts – for the reference case, the spherical model displays a maximum sinking velocity of 9 cm/yr, which is $\sim$ 1.3 cm/yr faster than the equivalent Cartesian case (Figure 4a,e); and (ii) the rate of trench retreat is higher for spherical models – the reference spherical case retreats $\sim$ 10% faster than its Cartesian counterpart (Figure 4b) and, as a result, the shape of the trench evolves differently, with curvature enhanced for spherical cases at a given stage of model evolution (Figure 5b).

3.2 Influence of subducting plate age

The two cases, W1200_young and W1200_old, were designed to demonstrate how plate thickness and density modify subduction dynamics. Our parameter values approximate younger (decreased $\Delta\rho$ and H) and older (increased $\Delta\rho$ and H) slabs, respectively.

The younger slab (W1200_young) stretches and sinks almost vertically through the upper mantle as it subducts, folding upon interaction with the transition zone (Figures

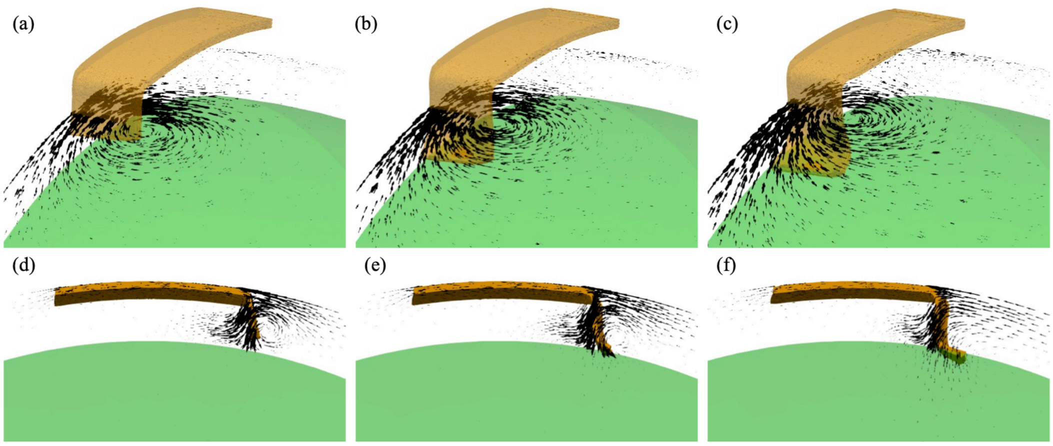

Figure 6. Snapshots of upper mantle flow regime from a spherical model at a plate width of 1200 km, plate thickness of 70 km and $\Delta\rho$ of 80 kg m^{-3}. (a)-(c) Tangential flow at 300 km depth, highlighting the toroidal flow cell at the edge of the plate. The largest arrows represent a tangential velocity magnitude of 3.7 cm/yr (radial component of velocity removed); (b)-(d) Poloidal flow cells, in the mantle wedge and sub-slab regions, at corresponding times. The largest arrow in the bottom panels represent velocity magnitude of 9.4 cm/yr. As the slab tip interacts with the mantle transition zone, the poloidal cell diminishes as the viscosity increase in the lower mantle prevents return flow beneath the slab tip.

3c,d and 4e). Trench location generally remains fixed (Figure 4b) and its shape does not evolve much over time (Figure 5a). Excluding the initial phase of subduction, trench retreat is minimal: within 5 Myr of subduction initiation, $\sim 80\%$ of subduction is accommodated by plate advance (Figure 4d).

The older case (W1200_old) exhibits the fastest sinking, trench retreat and plate advance velocities among all cases examined at this width (Figure 4). The slab tip sinks in the upper mantle at a shallower angle than the younger cases (Figure 4f). It is deflected at the mantle transition zone, and the sinking rate decreases as the slab moves into the lower mantle (Figure 4a,e). Similar to the reference case, after reaching the transition zone, the upper mantle portion of the slab gradually steepens (Figure 3e,f). Trench retreat is substantial and accommodates the majority of subduction (the trench retreat:total descent ratio remains above $\sim 55\%$ throughout the simulation – Figure 4b,d), with the trench developing a concave curvature over time (Figure 5c).

The cases examined at 1200 km width clearly display a range of behaviours, with a strong sensitivity to the thickness and density and, hence, age, of the subducting slab. The younger plate exhibits the weakest behaviour, manifest by a steeper upper mantle subduction angle and minimal trench retreat, with subduction principally accommodated via plate advance. This case falls into the vertical folding regime (e.g., Schellart, 2008; Stegman, Farrington, et al., 2010; Garel et al., 2014; Goes et al., 2017). The older plate is the strongest: it sinks faster, has a shallower upper mantle subduction angle, and drives significant trench retreat, with the majority of subduction accommodated via this retreat (Figure 4). This case falls into the weak retreat regime (e.g., Schellart, 2008; Stegman, Farrington, et al., 2010; Garel et al., 2014; Goes et al., 2017). As expected, the reference case has an intermediate strength, with sinking and trench-retreat rates, in addition to the slab dip angle, all between those of the older and younger cases (Figure 4). As trench

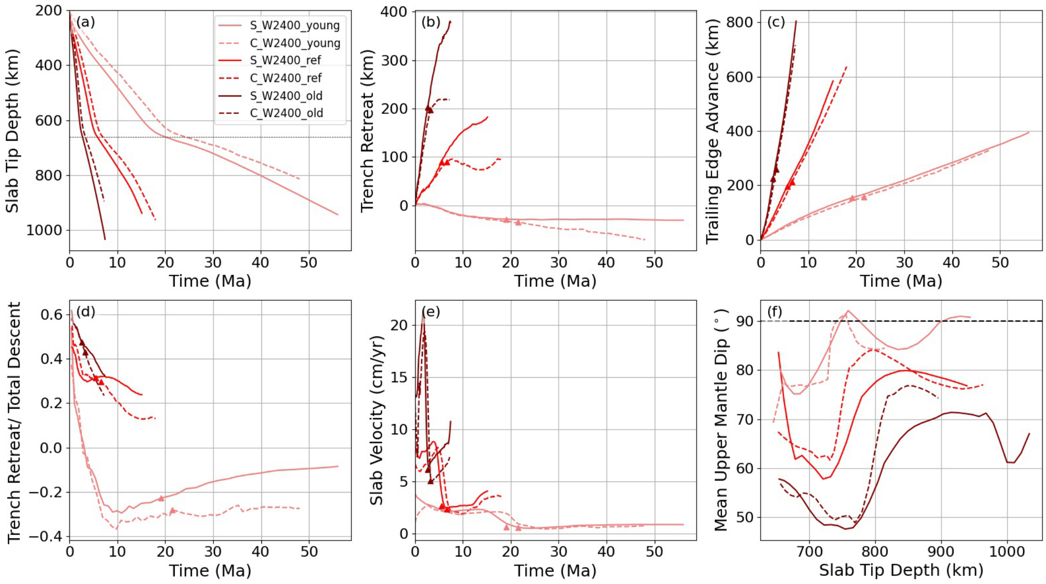

Figure 7. Comparison between spherical and Cartesian simulations with a plate width of 2400 km: (a) slab tip depth, as a function of time, where the upper–lower mantle boundary is indicated by the black dotted line at 660 km depth; (b) amount of trench retreat; (c) amount of plate advance, measured at the plate's trailing edge; (d) ratio of trench retreat to total descent, which is the sum of trench retreat and trailing edge advance; (e) slab sinking velocity; and (f) average slab dip in the upper mantle, with the black dashed line indicating a vertical slab with dip angle of 90°. Triangles indicate the time of slab tip transition-zone interaction. All measurements are taken at the symmetry plane.

retreat accounts for slightly more than $\sim 50\%$ of the total subduction in the reference case, it also falls into the weak retreat regime.

Although our spherical and Cartesian models are similar morphologically for the 1200 km wide plates, spherical models display consistently faster sinking rates than their Cartesian counterparts: the older case exhibits the greatest difference in maximum sinking velocity (~ 1.6 cm/yr) between comparable spherical and Cartesian cases, followed by the reference case (~ 1.3 cm/yr) and the younger case (~ 0.9 cm/yr). For the older and reference cases, which are both in the weak retreat regime, spherical models exhibit faster trench retreat rates than their Cartesian counterparts. The difference in trench velocity is negligible between the younger spherical and Cartesian cases, both of which fall into the vertical folding regime and display minimal trench motion.

3.3 Effect of subducting plate width

We next examine cases with the same density and thickness values as in the previous section, but at larger widths of 2400 km and 4800 km.

3.3.1 Less retreat

For cases that share a common plate age (thickness and density), a larger plate width reduces trench retreat. As the slab tries to maintain its sinking rate, this results in stronger bending at the trench. The dynamical behaviour can shift regimes, especially at the cen-

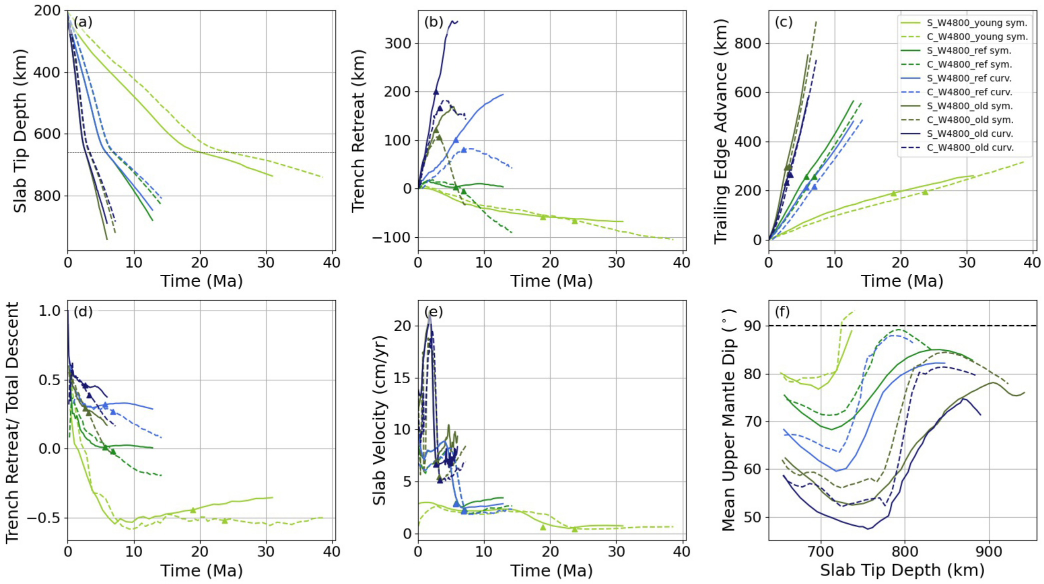

Figure 8. Comparison between spherical and Cartesian simulations with a plate width of 4800 km. Measurements are taken from the centre of the slab (i.e., the symmetry plane, abbreviated to sym.) and the location of most trench retreat, which is at the centre of the concave curvature (curv.).(a) slab tip depth, as a function of time, where the upper–lower mantle boundary is indicated by the black dotted line at 660 km depth; (b) amount of trench retreat; (c) amount of plate advance, measured at the plate's trailing edge; (d) ratio of trench retreat to total descent, which is the sum of trench retreat and trailing edge advance; (e) slab sinking velocity; and (f) average slab dip in the upper mantle, with the black dashed line indicating a vertical slab with dip angle of 90°. Triangles indicate the time of slab tip transition-zone interaction.

tre of the plate, where increased slab width causes slabs to steepen at the trench, with the trench sometimes advancing. The behaviour at the centre of the plate thereby shifts towards a 'bending mode', where slab bending at the trench takes up a significant part of the potential energy of the slab, as opposed to a 'sinking mode', where bending at the trench uses only 10-20% of the potential energy, and slab sinking is, in part, achieved through trench retreat (e.g. Capitanio et al., 2007; Ribe, 2010).

For younger cases, at both widths (W2400_young and W4800_young), slabs stretch and sink steeply in the upper mantle, at a dip of $> 75°$ (Figures 7f and 8f), eventually buckling upon interaction with the transition zone at 660 km depth (Figures 9c,d and 10c,d), like their narrower counterpart. However, as plate width increases, the rate of trench advance also increases. Upon interaction with 660 km, the 1200 km cases display minimal trench motion (Figure 4b), whereas the trench has advanced ~ 30 and ~ 50 km for the 2400 km and 4800 km wide cases, respectively (Figures 7b and 8b). This folding, with some advance, is a characteristic of a 'fold-and-retreat' bending mode (e.g., Schellart, 2008; Stegman, Farrington, et al., 2010; Goes et al., 2017), and the centre of wide young slabs display behaviour between a vertical folding and fold-and-retreat mode.

For wider cases at the reference age (W2400_ref and W4800_ref), slabs retreat prior to interacting with the transition zone. At the symmetry plane, they steepen and buckle following interaction (Figures 9a,b and 10a,b), thus demonstrating stronger bending at the trench in comparison to the 1200 km wide case, which displayed a deflect-and-sink

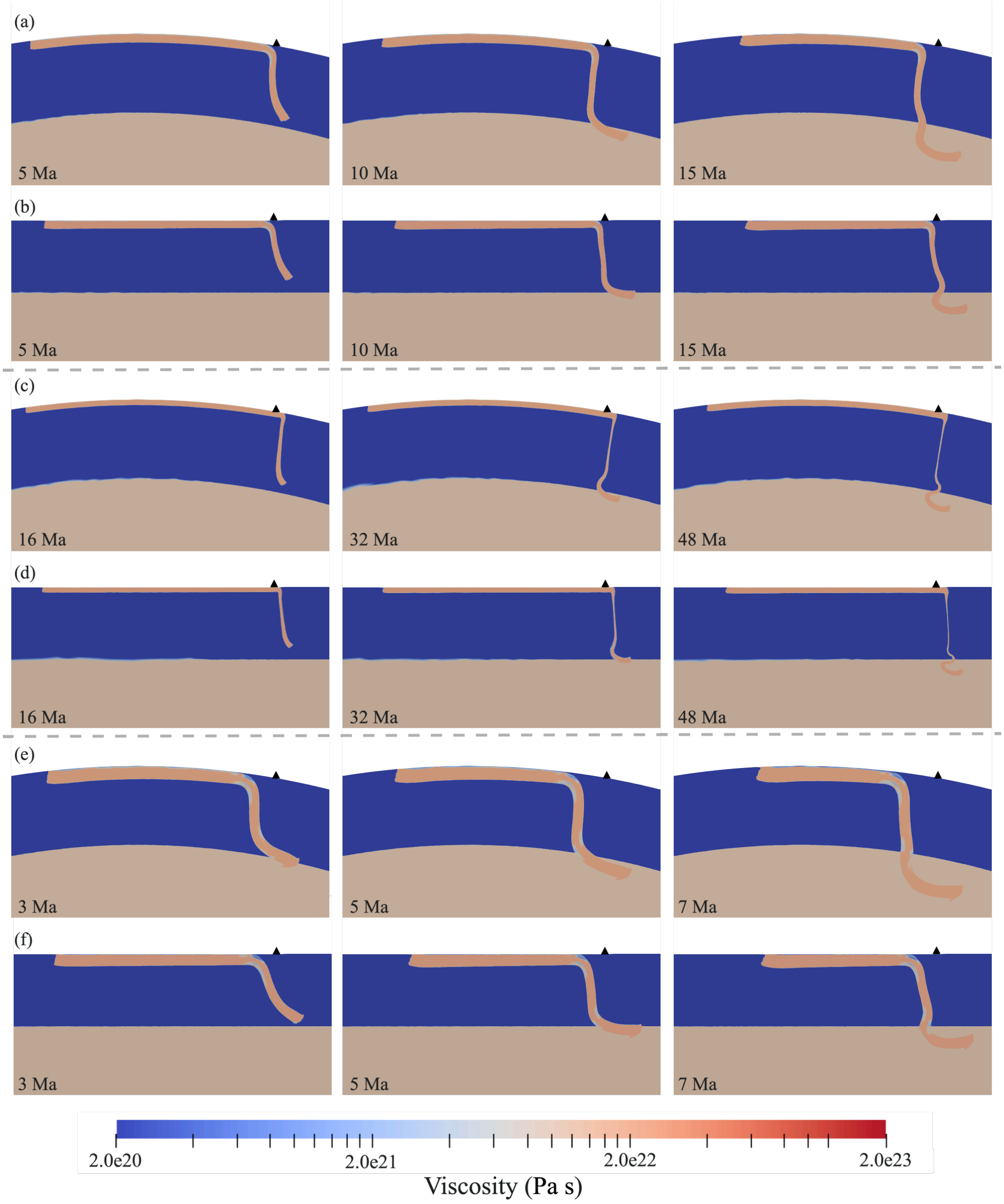

Figure 9. Snapshots illustrating the spatio-temporal evolution of slab morphology through the viscosity field, for spherical and Cartesian models with a plate width of 2400 km: (a) spherical; and (b) Cartesian cases, with $H = 70$ km and $\Delta\rho = 80\,\mathrm{kg\,m^{-3}}$; (c) spherical and (d) Cartesian models with $H = 45$ km and $\Delta\rho = 40\,\mathrm{kg\,m^{-3}}$; (e) spherical and (f) Cartesian models with $H = 100$ km and $\Delta\rho = 120\,\mathrm{kg\,m^{-3}}$.

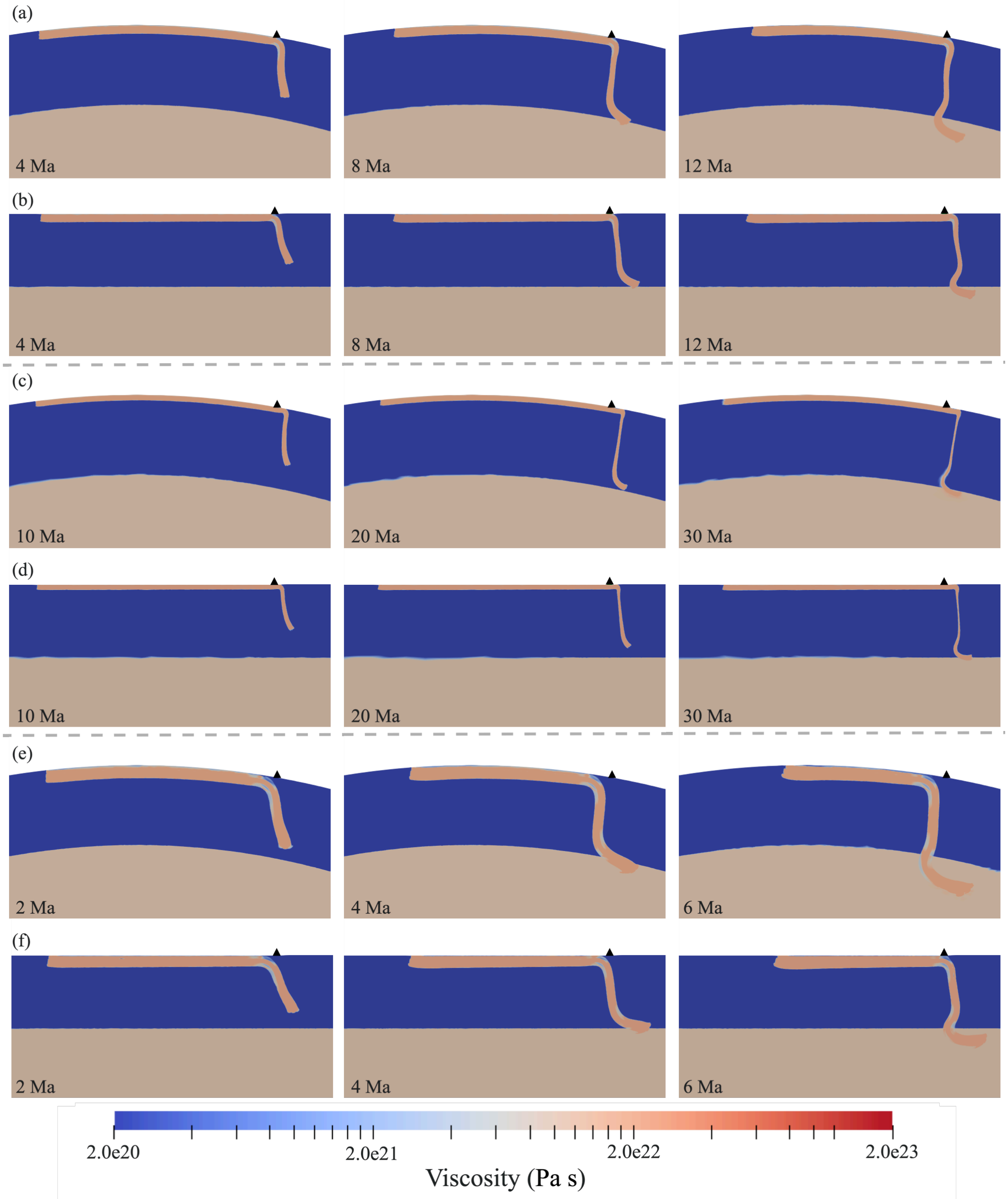

Figure 10. Snapshots illustrating the spatio-temporal evolution of slab morphology through the viscosity field, for spherical and Cartesian models with a plate width of 4800 km: (a) spherical; and (b) Cartesian cases, with $H = 70\,\mathrm{km}$ and $\Delta\rho = 80\,\mathrm{kg\,m^{-3}}$; (c) spherical and (d) Cartesian models with $H = 45\,\mathrm{km}$ and $\Delta\rho = 40\,\mathrm{kg\,m^{-3}}$; (e) spherical and (f) Cartesian models with $H = 100\,\mathrm{km}$ and $\Delta\rho = 120\,\mathrm{kg\,m^{-3}}$.

behaviour (Figure 3a,b). As plate width increases, the upper mantle portion of the slab steepens and the dip angle increases (Figure 4f, Figure 7f and Figure 8f). Buckled slabs with a width of 4800 km have maximum dips that exceed those of the 2400 km wide case by $\sim 4°$. At the symmetry plane, the trench retreat:total slab descent ratio decreases with plate width (~ 0.5 and ~ 0.2, for 1200 km and 2400 km wide cases, respectively, and $\sim -0.2 - 0$ for the 4800 km wide case), indicating less of a role for trench retreat in accommodating subduction. This is most clearly demonstrated for the Cartesian W4800_ref simulation, which transitions from retreat at a width of 1200 km, to advance at a width of 4800 km (Figures 4d, 7d and 8d).

For older cases at widths of 2400 km (W2400_old) and 4800 km (W4800_old), slabs sink with shallower angles than corresponding reference cases in the upper mantle (Figures 7f and 8f), deflecting at transition zone depths and, subsequently, sinking through into the lower mantle (Figures 9e,f and 10e,f). As plate width increases from 2400 km to 4800 km, the maximum upper mantle dip angle increases by $\sim 7°$. The trench retreat:total slab descent ratio also decreases as slab width increases, from ~ 0.6 to ~ 0.3 to < 0.2 for 1200 km, 2400 km and 4800 km wide slabs, respectively. The widest Cartesian case even exhibits trench advance, following slab transition-zone interaction. While the older 1200 km and 2400 km wide cases, in addition to the spherical 4800 km case, all fall into the weak retreat regime, the Cartesian W4800_old case begins to develop a buckling fold and shifts towards the vertical folding regime.

Taken together, our results demonstrate that as plate width increases, slabs display less of a tendency to retreat, as evidenced by a reduction in the trench retreat:total slab descent ratio across all three ages examined and, as a consequence, they bend more strongly at the trench.

3.3.2 Trench curvatures and along strike variations in morphology

Different trench shapes are observed across the simulations examined, which can be categorised into 3 types: (i) ‘I’-type, where the trench is reasonably straight (e.g., Figure 5a); (ii) ‘C’-type, where trench retreat is strongest in the centre of the slab relative to its edges (e.g., Figure 5b); and (iii) ‘W’-type, where trench retreat is low in the centre of the slab and at the edges, and higher in between (‘S’ curvature in half-width, as shown in Figure 12b).

We find that ‘I’-type trenches develop for younger cases across all plate widths: trenches remain reasonably straight, aside from a slight curvature adjacent to the slab edge (Figures 5a, 11a and 12a). ‘C’-type trenches develop for narrow plates that are retreating, for example, in cases W1200_ref and W1200_old (Figure 5b,c). For stronger plates that have moderate width, such as case W2400_old (Figure 11b), the trench develops a gentle curvature close to the edge, but the bulk of the trench remains approximately straight throughout the simulation, in an elongated ‘C’ shape. As slab width increases, ‘W’-type trenches develop on slabs that would have ‘C’-type trenches at a narrower width. This is exemplified by comparing cases W2400_ref and W4800_ref. Case W2400_ref develops a concave curvature at the edges, with the centre of the trench retreating slightly less than the edge (Figure 11b), placing it at the transition between ‘C’- and ‘W’-type trenches. Conversely, case W4800_ref displays a ‘W’-type curvature (Figure 12b). Similarly, for older slabs trenches develop into a ‘W’ shape (‘S’ in half-width in Figure 12 c). In case W4800_old, the curvature increases following slab transition-zone interaction and the difference in trench retreat between the centre and the region of most retreat also increases (Figure 8b).

Taken together, our results demonstrate that the evolution of trench shape is dependent on both slab age and slab width. Younger and weaker slabs that are in the vertical folding regime develop mostly straight ‘I’-type trenches, regardless of slab width. For older cases that can drive trench retreat, trench curvatures evolve from a ‘C’-shape

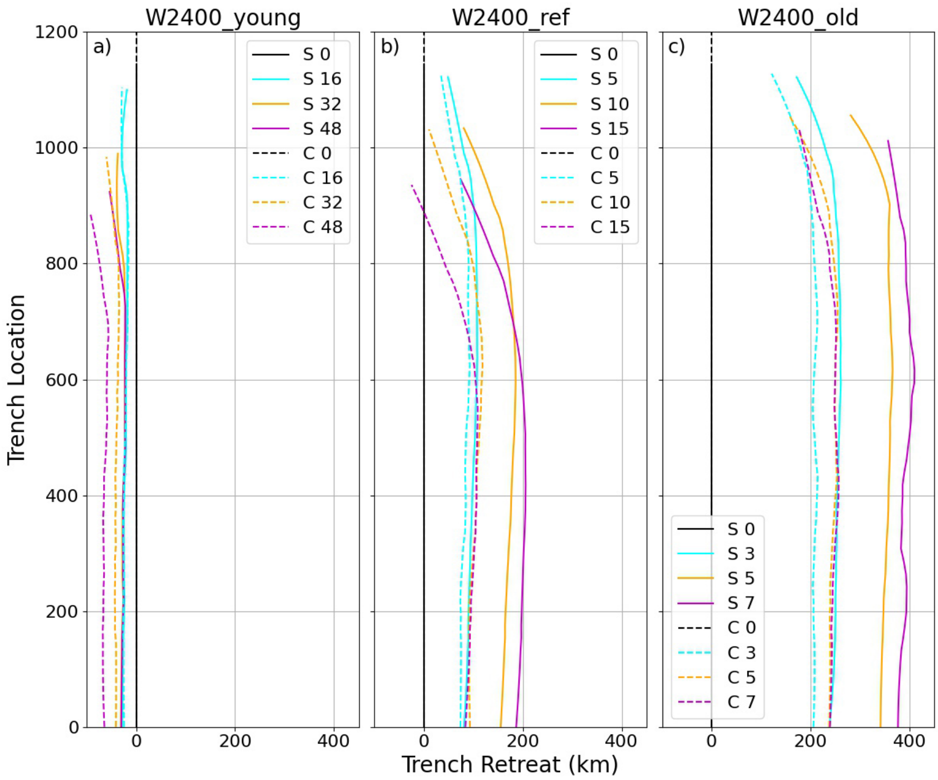

Figure 11. Spatio-temporal evolution of trench location in spherical (S, solid) and Cartesian (C, dashed) simulations, at a plate width of 2400 km. Times given in Myr since simulation initiation. (a) $H = 45\,\mathrm{km}$, $\Delta\rho = 40\,\mathrm{kg\,m^{-3}}$; (b) $H = 70\,\mathrm{km}$, $\Delta\rho = 80\,\mathrm{kg\,m^{-3}}$; (c) $H = 100\,\mathrm{km}$, $\Delta\rho = 120\,\mathrm{kg\,m^{-3}}$.

in narrower plates to a ‘W’-shape in wider plates, with slabs of greater strength transitioning to a ’W’ shape at a greater width.

Slab morphologies evolve with trench shape. For weaker cases with an ‘I’-type trench, subducting slab morphology is relatively uniform along strike (Figure 13a,d). For stronger wide retreating cases that develop a ’W’-type trench, along-strike variations in trench retreat translate into morphological variations at depth (Figures 13b,c,e,f and 8a): at the symmetry plane, the slab is steep and buckles at the transition zone, with dips up to 9° larger than the slab at the location of most retreat, which deflects at transition-zone depths (Figure 8d,f).

3.3.3 Spherical versus Cartesian

We find that, regardless of plate width, all spherical cases evolve faster than their Cartesian counterparts, displaying elevated descent rates. Retreating cases also display a shallower upper mantle dip angle (a difference of $\sim 5°$ for reference age slabs, and $\sim 3°$ for older slabs – Figures 7 and 8). In addition, we find that Cartesian cases are more prone to move into a bending mode with increasing plate width. For the younger advancing simulations, Cartesian trenches continue to advance at the same rate following slab transition-zone interaction, whereas the rate of trench advance is reduced in spherical cases. This leads to higher plate advance to total slab descent ratio for Cartesian models (Figures 7d and 8d), a characteristic of bending-mode subduction behaviour. For ref-

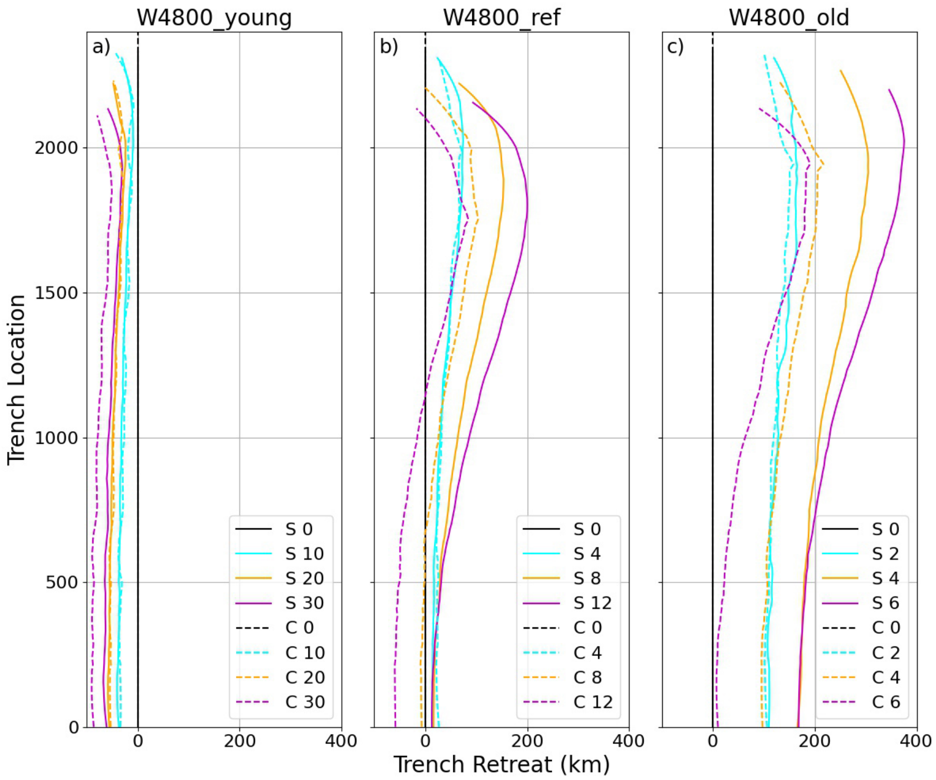

Figure 12. Spatio-temporal evolution of trench location in spherical (S, solid) and Cartesian (C, dashed) simulations, at a plate width of 4800 km. Times given in Myr since simulation initiation. (a) $H = 45\,\mathrm{km}$, $\Delta\rho = 40\,\mathrm{kg\,m^{-3}}$; (b) $H = 70\,\mathrm{km}$, $\Delta\rho = 80\,\mathrm{kg\,m^{-3}}$; (c) $H = 100\,\mathrm{km}$, $\Delta\rho = 120\,\mathrm{kg\,m^{-3}}$.

erence age simulations, the Cartesian case stops retreating after interaction with the transition zone at 2400 km width, and even switches from trench retreat to trench advance after reaching the lower mantle for the 4800 km width case (Figures 7b and 8b).

We find that a width of 2400 km is at the tipping point of the Cartesian reference model switching from a retreating regime to an advancing regime, after interaction at the transition zone. Spherical cases at this width, on the other hand, continue to retreat or stagnate after interacting with 660 km. The spherical W3600_ref model, however, exhibits trench advance at the symmetry plane after interaction with the lower mantle (Figure S2b). Taken together, this suggests that the tipping point from retreating to advancing for the spherical reference case is at an increased width of ~ 3600 km. At a width of 4800 km, the trench at the symmetry plane of the Cartesian case advances but, in comparison, the spherical cases behave stronger, evolving with ongoing trench retreat (Figure 8b). For older cases, only the Cartesian 4800 km case develops buckling at the centre of the slab due to its steep angle when hitting the transition zone; the corresponding spherical case, although steepened, remains sufficiently strong to resist vertical folding (Figure 10e,f). The strength of the spherical plate is large enough that the increased resistance to slab rollback does not fully hamper trench retreat. For 4800 km wide cases, after interaction with the viscosity jump at 660 km, the spherical case continues to retreat without slowing down significantly, but the Cartesian case stops retreating at the symmetry plane (Figure 8b). Overall, as slab width increases, the weaker behavior of Carte-

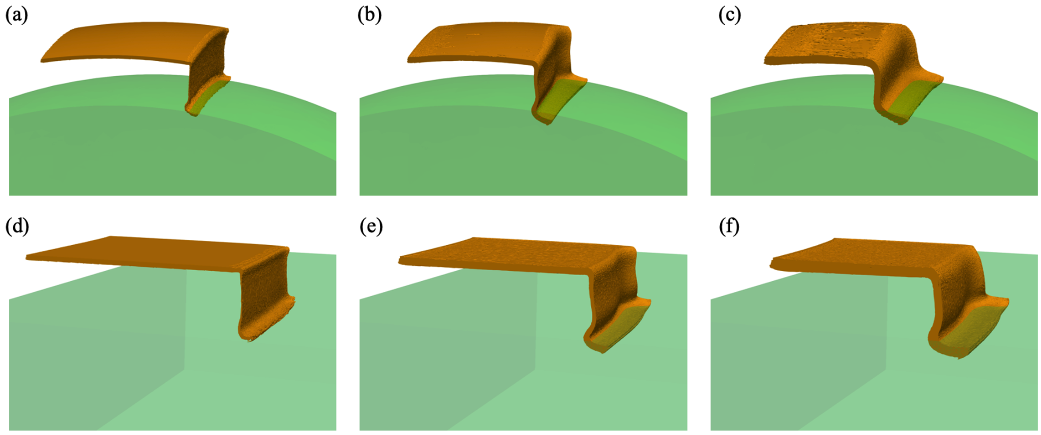

Figure 13. 3-D morphology of spherical (top) and Cartesian (bottom) cases at a width of 4800 km: (a/d) $H = 45\,\mathrm{km}$, $\Delta\rho = 40\,\mathrm{kg\,m^{-3}}$; (b/e) $H = 70\,\mathrm{km}$, $\Delta\rho = 80\,\mathrm{kg\,m^{-3}}$; (c/f) $H = 100\,\mathrm{km}$, $\Delta\rho = 120\,\mathrm{kg\,m^{-3}}$. Younger cases (a,d) has relatively uniform morphology along-strike, whereas older cases (b,e,f) have different morphologies: vertically folding at the centre, but horizontally deflect closer to the edge. The spherical cases develop less prominent along-strike variations in morphology than cartesian cases (b,e and c,f)

sian cases relative to their spherical counterparts becomes more prominent (as outlined in section 3.3.1).

Wider spherical and Cartesian cases also develop significant differences along-strike. For example, in Case W4800_ref, the centre of concavity (location of most trench retreat) continues to retreat after interaction with the transition zone in the spherical model, but for the Cartesian case, despite initially retreating more than the centre of plate, it switches to advancing after slab transition-zone interaction (Figure 8b). The differences in retreat rates and dip angles (Figure 8) lead to different along-strike slab morphologies between Cartesian and spherical models, as illustrated in Figure 13(b,e). Overall, Cartesian models display more dramatic along strike variations in morphology than spherical models.

4 Discussion

4.1 Role of Subducting Plate Age and Width

Our results demonstrate that the evolution of subduction systems is strongly sensitive to slab density and thickness (age), which is consistent with several previous studies (e.g., Capitanio et al., 2007; Schellart, 2008; Stegman, Farrington, et al., 2010; Garel et al., 2014). Higher density slabs increase slab pull, which increases upper mantle sinking velocities (e.g., Stegman, Farrington, et al., 2010; Garel et al., 2014; Goes et al., 2017). Slab thickness determines slab strength (and buoyancy), with thicker slabs possessing a higher bending resistance (e.g., Conrad & Hager, 1999; Bellahsen et al., 2005; Ribe, 2010; Capitanio & Morra, 2012) and, accordingly, taking longer to bend at the trench. The regime that a subduction system falls into depends on a delicate balance between the amount of time taken to bend (larger for thicker slabs) and the sinking time (larger for younger slabs). Taken together, in younger slabs (low slab pull – longer sinking times; low slab strength – shorter bending times), bending dominates over trench retreat, with slabs typically subducting steeply and buckling upon interaction with the mantle transition zone, owing to the high angle of incidence. Conversely, in older slabs (high slab

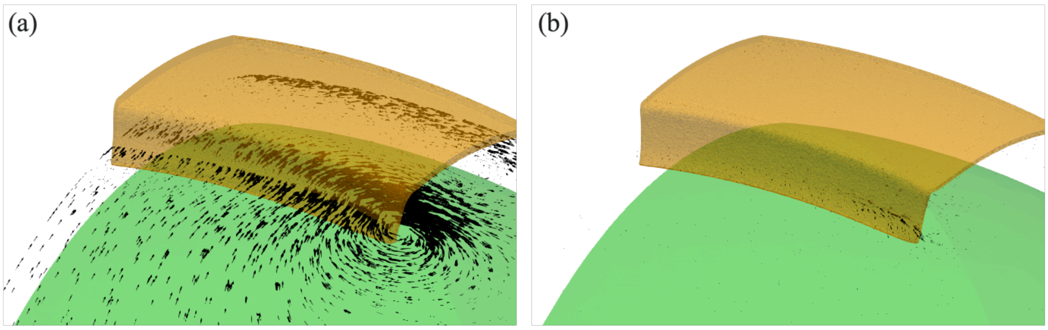

Figure 14. Lateral flow patterns at 300 km depth for: (a) case S_W4800_ref; and (b) case S_W4800_young. The length and direction of the arrows illustrates the magnitude and direction of tangential velocities (i.e. after the radial component has been removed). In both panels, the largest arrow represents a tangential velocity magnitude of 2.5 cm/yr. For the reference age case in (a), a toroidal cell can be identified at the edge of the slab, which has a limited area of influence, and does not affect the centre of the slab. For the younger case in (b), although there is some toroidal flow around the edge of the slab, its magnitude and influence is insignificant when compared to the reference case.

pull – shorter sinking times; high slab strength – longer bending times), there is insufficient time for substantial bending at the trench, with subduction accommodated principally through trench retreat. As a a result, slabs typically exhibit a shallower upper mantle dip angle, which prevents slab buckling at the transition zone: the lower the dip angle, the more easily slabs can deflect and stagnate at these depths (e.g., Torii & Yoshioka, 2007; Čížková & Bina, 2013; Garel et al., 2014; Agrusta et al., 2017).

The evolution of 'C'- and 'W'-trench shapes for our retreating cases are similar to results from Schellart et al. (2007), with curvature at slab edges induced by toroidal flow into the slab. Interplay between the size and strength of the toroidal cell, the width of the slab, and the slab's tendency to bend, dictate how the trench responds. The size of the toroidal cell determines the location along the trench that is experiencing the largest force from adjacent mantle flow and, hence, the location of the potential concave curvature development. The strength of the toroidal cell is determined by slab pull which, in turn, determines the strength of forces acting at the trench, whilst the width of the plate relative to the size of the toroidal cell determines the distance between the toroidal cells at both edges. When these factors are coupled with the the plate's resistance to bending, the evolution of trench shape can be determined. 'C'-shaped trenches are observed for narrow plates, where toroidal cell sizes are almost half of the slab width (Figure 6). 'W'-shaped trenches are observed for wider plates, where the size of the toroidal cell is substantially smaller than the width of the plate: the centre of such plates are thus not markedly influenced by toroidal flow (Figure 14a). Plates with higher bending resistance, which drive trench retreat, can develop enhanced curvature (W4800_ref, Figure 12b); conversely, plates with a low strength can prevent significant curvature development, remaining in an 'I'-shape or elongated 'C'-shape rather than evolving into a 'W'-shape (e.g., W2400_old, Figure 11c).

While the influence of plate width on subduction dynamics has been carefully studied (e.g., Stegman et al., 2006; Schellart et al., 2007; Di Giuseppe et al., 2008), our results demonstrate that the important role of width is strongly modulated by the age of the plate and its effective strength. The change from a 'C'-shaped trench to a 'W'-shaped trench with increasing width only occurs for cases that are initially in a retreating regime

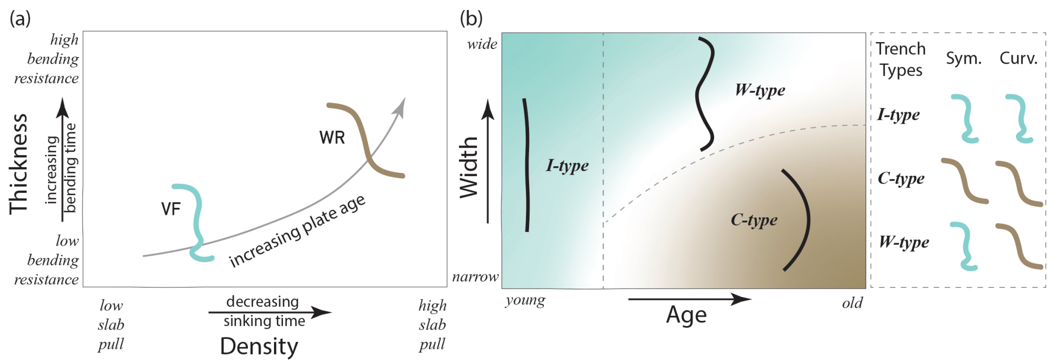

Figure 15. Schematic diagrams of how (a) density and thickness (adapted from Goes et al. (2017); and (b) age and width, affect subduction styles and trench shape. Regimes: VF - vertical folding; WR - weak retreat. In (a), slabs with higher density have higher slab pull and, accordingly, a reduced upper mantle sinking time. Thicker slabs have more bending resistance and, thus, require more time to bend. Older plates, which are thicker and denser, are able to drive more trench retreat as they have less time to bend. In (b), the three trench types 'I', 'C' and 'W' are separated into three approximate domains, by gray dashed lines, with slabs that lie on domain boundaries at the transition between two trench types. Slab behaviours that are in VF at the symmetry plane are represented by the cyan region, and those in WR are represented by the brown region. The rightmost panel illustrates the slab morphology at the centre of the slab (i.e., the symmetry plane, abbreviated to sym.) and the location of most trench retreat, which is at the centre of the concave curvature (curv.). For young plates, the subduction regime is VF regardless of the width of the plate, and trench shapes are mostly straight, indicated by 'I'-type. As age increases, it is easier to drive trench retreat and slabs fall into the WR regime; but as width increases, the centre of the plate shifts towards the VF regime. Beyond a certain age, the narrower and/or older plates tend to develop 'C'-type trenches; wider and/or younger plates tend to develop 'W'-type trenches.

(i.e., the older plates). For younger plates that are in the vertical folding regime, increasing plate width has little impact on along-strike variability, because the low slab pull and slow upper mantle sinking rates of younger plates are insufficient to generate toroidal cells of the intensity required to induce trench deformation (Figure 14b). Accordingly, the younger cases develop 'I'-type trench shapes across all widths examined in this study (in both Cartesian and spherical geometries).

Variations in the amount of trench retreat also translate into along-strike morphological variations at depth: the centre of wider slabs are categorised into the vertical folding regime, with steep to overturned upper mantle dips and folding at 660 km depth, whereas in the parts of the slab where the trench retreats most, they subduct in a weak retreat regime with shallower dips and deflect at the transition zone. The lack of toroidal flow influence at the centre of wider slabs reduces the slab's ability to retreat, which encourages more bending at the trench, leading to steeper slabs that buckle at the transition zone. While all wide slabs display the typical morphology of the vertical folding regime at the centre, the young models have tight buckles, whereas older slabs have open folds with larger bending radii. This difference in bending radii illustrates that older slabs have higher bending resistance and strength than younger slabs, despite falling into the same subduction regime. Overall, as plate width increases, the center of the slab shifts from sinking to bending, due to the lack of toroidal flow and its role in driving trench retreat.

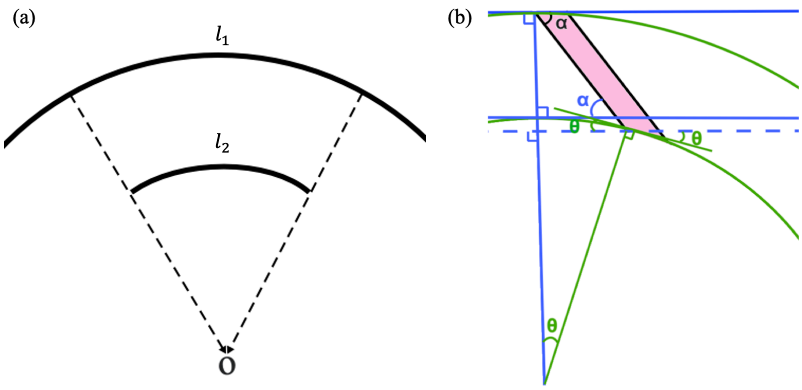

Figure 16. Key geometrical features of a spherical geometry that influence subduction evolution when compared to a Cartesian geometry: (a) the spherical geometry concentrates material as it sinks radially towards the centre of the sphere. Bounded by the same radial lines, the length l_2 at depth is shorter than l_1 at the surface. For a 3-D sphere, the tangential area decreases as depth increases (the mantle closes upon itself), concentrating subducting materials; (b) the curvature of the sphere causes the apparent dip of a descending feature to decrease relative to an internal interface. The example is a straight slab of dip α intersecting the lower mantle in Cartesian and spherical setups (distance is not to scale). The slab forms an angle of α with the lower mantle in the Cartesian domain (illustrated in blue). In the spherical domain (illustrated in green), the tip of the slab traveled an angular distance of θ to reach the lower mantle, and forms an angle of $(\alpha - \theta)$ with the curved interface at the point of intersection. The angle of difference (θ) due to the curvature is $\sim 5^\circ$ for plates with an upper mantle dip (α) of 60°.

The competing role of plate age and plate width in dictating the subduction style are summarised via a regime diagram in Figure 15. As plate age (density and thickness) increases, the plate behaves more strongly and transitions from a vertical folding regime at younger ages to a weak retreat regime regime at older ages. As slab width increases, along strike variations in slab morphology can develop due to differences in the amount of trench retreat. Younger slabs develop 'I'-type trenches across all widths. Conversely, retreating older cases develop 'C'-type trenches at narrower widths, and 'W'-type trenches for wider cases, with a transitional 'C\W'-type at intermediate plate age and width. The critical width where trenches transition from 'C'-type to 'W'-type depends on plate age: the older (stronger) the plate, the greater the slab width required to develop 'W' shapes.

4.2 The Importance of Sphericity

One of the most significant differences between spherical and Cartesian geometries is the direction of gravity: in spherical domains, gravity acts in the radial direction towards the centre, whereas in Cartesian simulations, the direction of gravity is constant across the entire domain. As illustrated in Figure 16(a), an object of length l_1 sinking on a sphere in the direction of gravity must reduce its length according to the reduction in radius to maintain the same subtended angle. On Earth, by the time a slab sinks from the surface to 660 km depth (l_2), its lateral dimensions will be reduced by $\sim 10\%$. This is a significant amount of shortening that causes buoyancy to concentrate as the mantle closes in upon itself.

This concentration of buoyancy increases slab pull and drives faster sinking, thus reducing the time available for bending at the trench. As a result, subduction tends to be accommodated through more trench retreat, with the slab descending at a shallower dip angle. This partially explains why slabs trend towards stronger behavior on a sphere.

To fit the curved surface of a sphere, slabs are bent around two orthogonal axes. This double curvature increases the geometric stiffness of slabs, which are subsequently able to resist bending and deformation (Mahadevan et al., 2010): the curvature of the spherical surface therefore increases the stiffness of a subducting slab. As a result, slabs in a spherical domain require more time to bend at the trench than their Cartesian counterparts. This, combined with the reduced sinking time due to geometrically concentrated buoyancy, leads to slabs in spherical models having a greater effective strength. The geometric stiffness and stronger effective strength acts against along-strike deformations, as exemplified by the less amplified 'W'-shaped curvature of trenches in wider spherical cases relative to their Cartesian counterparts.

Slab interaction with the transition zone is also influenced by the spherical geometry. The internal interfaces of a sphere, such as the mantle transition zone, are smaller concentric spheres. As such, the mantle transition zone curves away from the descending slab at the point of impingement, as illustrated in Figure 16(b). The angle of interaction of a slab with the curved mantle transition zone is shallower by the angular distance, θ, travelled by the slab tip, compared to a parallel slab that is in a Cartesian domain, where lateral movement of the slab tip does not affect the angle of incidence. This will enhance trench retreat in a spherical domain, as the lower the dip angle, the more easily slabs can deflect or stagnate on the transition zone (e.g., Christensen, 2001; Torii & Yoshioka, 2007; Tagawa et al., 2007).

To summarise, both spherical and Cartesian models exhibit a range of slab morphologies and trench curvatures, similar to those predicted in previous studies (e.g., Schellart, 2008; Stegman, Farrington, et al., 2010; Garel et al., 2014). However, plates on a sphere behave more strongly than plates in a Cartesian domain due to the spherical geometry. The effect of sphericity becomes more significant for wider plates, being similar to increasing plate age for Cartesian models. Hence, Cartesian models can capture the key features of subduction dynamics for narrower plates, but are less suitable for modelling subduction for wider plates. Our results suggest that this limit is approximately 2000 km.

4.3 Implications for Subduction on Earth

Our results, across different plate thicknesses, densities and widths, allow us to analyse how plate age and width combine to control the spatio-temporal evolution of trenches on Earth. While Earth's subduction zones are substantially more complex than those considered in our models, due to a multitude of factors including subducting plates of non-uniform age, the subduction of buoyant anomalies, and the influence of overriding plates, the 'I', 'C' and 'W' trench shapes predicted by our models are consistent with present-day trench shapes (e.g. Heuret et al., 2011; Müller et al., 2016) and those in reconstructions of plate motion histories through the Cenozoic Era (Müller et al., 2019).

4.3.1 'I'-type Trenches

Our results demonstrate that 'I'-shape trenches typically develop when a young plate subducts with negligible trench motion, regardless of trench width. The tectonic reconstructions of Müller et al. (2019) provide some examples of young plate subduction during the Cenozoic, into the Japan subduction zone at $50-60$ Ma and the Farallon (North American) subduction zone prior to ~ 30 Ma (Figure 17).

As illustrated in Figure 18, the Japan subduction zone was relatively straight (apart from its northern end) with minimal trench motion between 50 and 60 Ma, characteristics typical of 'I'-type trenches. The trench measured ~ 5000 km in width, and a young

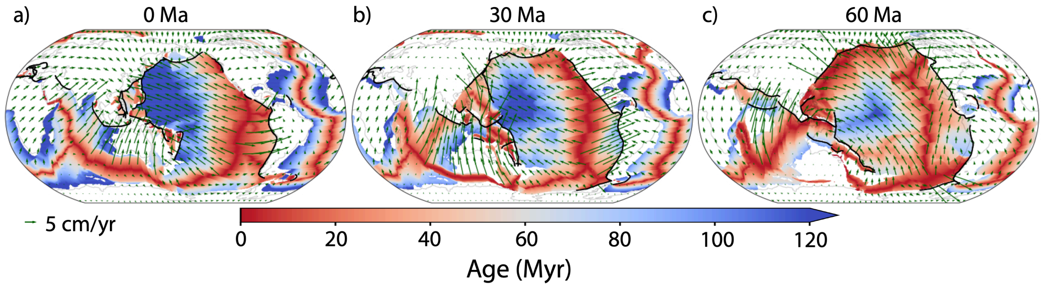

Figure 17. Maps of ocean-floor age based on plate reconstruction by Müller et al. (2019) at: (a) the present-day; (b) 30 Ma; and (c) 60 Ma. Green arrows represent plate velocity (in the mantle reference frame of the reconstruction). Trenches are shown as black lines and present day coastlines are shown in light grey(Met Office, 2010 - 2015).

plate ($\sim$ 10 Myr) was subducted along the whole trench (Figure 17c). As time advanced past 30 Ma, the main part of the trench evolved from an 'I'-type towards a 'C'-type example, with increasing trench retreat, trench curvature and trench segmentation (Figure 18a). This is coincident with an increase in subducting plate age, as shown in Figure 17(a,b).

Similarly, for Farallon subduction (North America), the reconstructed trench has an 'I'-type shape prior to 30 Ma, when the very young ($\sim$ 10 Myr at 30 Ma) Farallon plate was subducting beneath North America, as shown in Figure 17(b). Prior to 30 Ma, the trench shape was relatively straight, with very little trench retreat, particularly from 30$-$50 Ma (Figure 18). Following breakup of the Farallon Plate in the mid-Cenozoic, into the Juan de Fuca, Cocos and Nazca Plates (e.g., Atwater, 1970; Lonsdale, 2005), the continuity of the 5900 km-wide trench was lost, and the strike-slip San Andreas Fault developed on the west coast of North America.

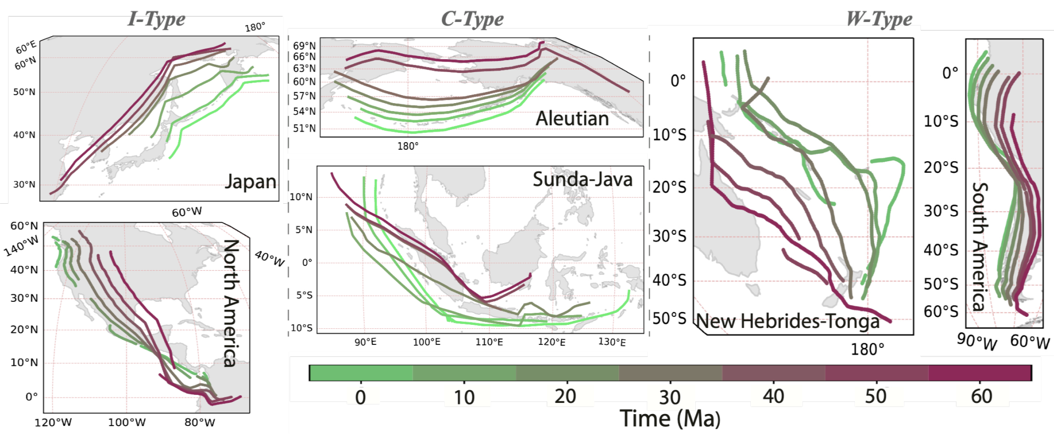

Figure 18. Examples of 'I' shape (a), 'C' shape (b) and 'W' shape (c) trenches based on the plate reconstruction by Müller et al. (2019), where trenches are drawn at 10 Myr intervals.

4.3.2 'C'-type Trenches

Our results suggest that 'C'-shape trenches should be associated with moderate to old subducting plate ages and moderate slab widths. 'C'-shape trenches are the most common trench shape observed on Earth. The Aleutian subduction zone and the Sunda-Java subduction zone are two examples of 'C'-shape trenches that developed through the Cenozoic (Figure 18). Although both trenches have also been affected by buoyant structures on the incoming plate (such as Yakutat terrane below Alaska and Australian continental crust impinging on the Banda part of the Sunda-Java arc), we propose that the combined width and age of the downgoing plate significantly affected the evolution of trench shape.

The Aleutian trench extends ~ 4000 km from the south coast of Alaska to Kamchatka (Scholl et al., 1975). At 60 Ma, young material ($\sim 10-40$ Myr) was subducted along the trench (Figure 17b); as a result, between 50 and 60 Ma, the trench shape remained relatively unchanged, with only a gentle curvature, with a shape between 'C'- and 'I'-types (Figure 18, Müller et al., 2019). As time progressed, the age of the subducting plate increased and the Aleutian trench retreated and developed a 'C'-shape curvature, with enhanced curvature in the west (Figure 18). This is consistent with our modelling predictions, and could be related to the non-uniform subducting plate age at the Aleutian trench: the subducting Pacific plate is younger to the east (currently ~ 10 Myr) and older to the west (~ 120 Myr at present, Figure 17a,b), with the older part of the plate driving more retreat, generating the asymmetric 'C'-shaped trench.

The Sunda-Java trench also has a complex subduction history. Prior to 43 Ma, the active Wharton ridge was subducting beneath Sumatra, but since then the ridge has become inactive (Whittaker et al., 2007). As a result, the majority of material subducted prior to 43 Ma was young (~ 10 Myr old – Figure 17c), leading to minimal trench motion at the Sunda-Java subduction zone, consistent with 'I'-type subduction (Figure 18b). As the Wharton ridge ceased spreading and the subducting plate age increased (Figure 17a,b), the trench began to retreat and developed a 'C' shape across its ~ 5000 km width, again demonstrating that an 'I'-type to 'C'-type transition can occur when subducting plate age increases, consistent with our modelling predictions.

4.3.3 'W'-type Trenches

'W'-type trenches develop with moderate and older subducting plate age and very wide trenches. The South American trench is the textbook example of a 'W'-shape (Schellart et al., 2007): it exhibits concave curvature on both edges, with the centre of the trench almost stagnant throughout the Cenozoic (Figure 17c). Subduction in the South Pacific also exhibits 'W'-type characteristics in the early Cenozoic.

The South American trench is over 6000 km long, and subducted moderately old material ($\sim 50-80$ Myr) throughout the Cenozoic at the centre of the trench (Figure 17). Trench evolution shows increasing oroclinal bending through the Cenozoic (Schepers et al., 2017) and, hence, more retreat towards the north and south than in the central part at the Bolivian bend (Figure 18, Müller et al., 2019). The present-day trench shape is typical of our wide plate model predictions, where the Bolivian Orocline protrudes close to the centre of the trench, while sections of the trench close the edges have a concave geometry. The subduction of pre-existing buoyant features on the Nazca Plate likely add complexity to the explanation of its evolution towards the current geometry (e.g., Gutscher, Olivet, et al., 1999; Espurt et al., 2008). The age pattern of the downgoing Nazca Plate and the thickness of the upper plate also potentially influence the orocline, as the topographic symmetry of the Andean mountain belt around Central Andes coincides with the younging of Nazca plate to both north and south directions from Central Andes and the thinning of the upper plate from the center towards the north and south (Capitanio et al., 2011). Thus although it is likely that multiple factors contribute to the shape of the trench at the South America Subduction Zone, our results suggest that the first-order 'W'-shape is dictated by its large width and moderate subducting-plate age.

The South Pacific region has a more complex tectonic history. In the early Cenozoic, the old Pacific plate was subducting under the South Pacific trench, which had length exceeding 6000 km (Figure 17c). The trench shape at 60 Ma resembles 'W'-shape trenches, where the oldest (~ 100 Myr) part of the plate was subducting at a region of least trench retreat, in the northern part of the trench. It had the middle 'stagnation' and the southern concave part of the 'W'-shape, where as the northern concave curvature is not clearly observed, partly due to the complex tectonic settings to the north (Figure 18, 17c). Here too, buoyant features, in particular the Ontong-Java plateau (Neal et al., 1997; Mann & Taira, 2004; Stotz et al., 2017) affected the segmentation of the trench into the New Hebrides, New Britain and Tonga-Kermadec-Hikurangi trenches (e.g., Pelletier et al., 1998). However, the shape of the resulting trenches was likely preconditioned by the original 'W' shape.

Overall, the examples of 'I'-, 'C'- and 'W'-shape trenches on Earth are in line with our modeling results. 'I'-type trenches are associated with very young downgoing plates of ~ 10 Myr old; and as plate age increases, some transition into 'C'-shape trenches. 'W'-shape trenches are observed in subduction zones exceeding 6000 km width, where older material (greater than 50 Myr old) is being subducted, thus driving trench retreat. There is no doubt that the trench shape at each subduction zone is further modulated by additional complexities, including variable downgoing plate age along strike, subduction of buoyant active or bathymetric ridges, and variations in thickness and buoyancy of the upper plate. Nonetheless, our results demonstrate the key role that both subducting plate age and width play in controlling the evolution of trench geometry, providing a framework to better understand the evolution of subduction zones.

5 Conclusions

We have presented new 3-D spherical free-subduction models with a composite visco-plastic plate and viscously layered mantle. We examined the sensitivity of subduction dynamics and trench evolution to different plate ages (simulated with covarying plate densities and thicknesses) and plate widths, in both spherical and Cartesian settings.

Our models show similar results to previous studies on the effect of age and width on the evolution of the subduction zone. As plate age increases, plate strength increases and, as a result, the subduction style transitions from vertically sinking and folding to retreating with a shallower upper mantle dip angle. Our models produce 'C' shaped trenches for narrower plates and 'W' shaped trenches for wider plates, resulting from the toroidal flow cells at the edge of the retreating subducting plates, consistent with the models of Schellart et al. (2007). However, we also find that the effect of width is modulated by the age of the subducting plate. For young plates that are in the vertical folding regime, the trench does not develop a 'W' shape, even for very wide plates. The trench only develops 'C' or 'W' shapes for retreating cases. Furthermore, for plates that are in the retreating regime, a younger plate develops more along-strike variability than an older plate, due to its lower strength.

We find that spherical geometry increases the effective strength of the plate due to three main factors: (i) the spherical geometry concentrates the buoyancy of subducted material, leading to faster sinking rates and, accordingly, reducing the time available for bending at the trench; (ii) the curvature of the mantle transition zone further reduces the effective dip angle when interacting at 660 km, whereby the slab has more tendency to retreat and deflect at the transition zone; and (iii) the double curvature of the plate on a spherical surface adds mechanical strength that resists bending, which is particularly important for wider plates and the evolution of their trenches.

Although Cartesian simulations are sufficient to capture the subduction dynamics of narrow plates (less than approx. 2000 km in width), we now have the means to more accurately simulate subduction dynamics on a sphere. This opens up new possibilities and will be used in the future to investigate additional factors that affect subduction dynamics and their expression at Earth's surface.

Acknowledgments

F.C. is funded by an Australian Government Research Training Program (RTP) Scholarship. D.R.D. acknowledges support from the Australian Research Council (ARC), under DP170100058. L.S. was funded by an EPSRC DTP studentship (EP/N509486/1), S.G. received support under NERC grant NE/K010743/1. Numerical simulations were undertaken on the NCI National Facility in Canberra, Australia, which is supported by the Australian Commonwealth Government. The Fluidity computational modelling framework, including source code and documentation, is available from `https://fluidityproject.github.io/`; the version used for the simulations presented herein has been archived at https://zenodo.org/record/5636819#.YYBeydZBxR4. Authors would like to thank Cian Wilson, Chris Matthews, Thomas Duvernay, Siavash Ghelichkhan, Angus Gibson and Marthe Klöcking for fruitful discussions at various stages of this research.

References

Agrusta, R., Goes, S., & van Hunen, J. (2017). Subducting-slab transition-zone interaction: Stagnation, penetration and mode switches. *Earth and Planetary Science Letters*, *464*, 10–23.

Atwater, T. (1970). Implications of plate tectonics for the Cenozoic tectonic evolution of western North America. *Geological Society of America Bulletin*, *81*(12), 3513–3536.

Balay, S., Gropp, W. D., McInnes, L. C., & Smith, B. F. (1997). Efficient management of parallelism in object-oriented numerical software libraries. In *Modern software tools for scientific computing* (pp. 163–202). Birkhauser Boston Inc.

Bellahsen, N., Faccenna, C., & Funiciello, F. (2005). Dynamics of subduction and plate motion in laboratory experiments: Insights into the "plate tectonics" behavior of the Earth. *Journal of Geophysical Research: Solid Earth*, *110*(B1).

Butterworth, N. P., Quevedo, L., Morra, G., & Müller, R. (2012). Influence of overriding plate geometry and rheology on subduction. *Geochemistry, Geophysics, Geosystems*, *13*(6).

Butterworth, N. P., Talsma, A. S., Müller, R. D., Seton, M., Bunge, H.-P., Schuberth, B. S. A., ... Heine, C. (2014). Geological, tomographic, kinematic and geodynamic constraints on the dynamics of sinking slabs. *Journal of Geodynamics*, *73*, 1–13.

Capitanio, F. A., Faccenna, C., Zlotnik, S., & Stegman, D. R. (2011). Subduction dynamics and the origin of Andean orogeny and the Bolivian orocline. *Nature*, *480*(7375), 83–86.

Capitanio, F. A., & Morra, G. (2012). The bending mechanics in a dynamic subduction system: Constraints from numerical modelling and global compilation analysis. *Tectonophysics*, *522*, 224–234.

Capitanio, F. A., Morra, G., & Goes, S. (2007). Dynamic models of downgoing plate-buoyancy driven subduction: Subduction motions and energy dissipation. *Earth and Planetary Science Letters*, *262*(1-2), 284–297.

Capitanio, F. A., Stegman, D. R., Moresi, L. N., & Sharples, W. (2010). Upper plate controls on deep subduction, trench migrations and deformations at convergent margins. *Tectonophysics*, *483*(1-2), 80–92.

Christensen, U. (2001). Geodynamic models of deep subduction. *Physics of the Earth and Planetary Interiors*, *127*(1-4), 25–34.

Čížková, H., & Bina, C. R. (2013). Effects of mantle and subduction-interface rheologies on slab stagnation and trench rollback. *Earth and Planetary Science Letters*, *379*, 95–103.
Čížková, H., van Hunen, J., & van den Berg, A. (2007). Stress distribution within subducting slabs and their deformation in the transition zone. *Physics of the Earth and Planetary Interiors*, *161*(3-4), 202–214.
Čížková, H., van Hunen, J., van den Berg, A. P., & Vlaar, N. J. (2002). The influence of rheological weakening and yield stress on the interaction of slabs with the 670 km discontinuity. *Earth and Planetary Science Letters*, *199*(3-4), 447–457.
Conrad, C. P., & Hager, B. H. (1999). Effects of plate bending and fault strength at subduction zones on plate dynamics. *Journal of Geophysical Research: Solid Earth*, *104*(B8), 17551–17571.
Cross, T. A., & Pilger, R. H. (1982). Controls of subduction geometry, location of magmatic arcs, and tectonics of arc and back-arc regions. *Geological Society of America Bulletin*, *93*(6), 545–562.
Davies, D. R., Le Voci, G., Goes, S., Kramer, S. C., & Wilson, C. R. (2016). The mantle wedge's transient 3-D flow regime and thermal structure. *Geochem. Geophys. Geosys.*, *17*, 78-100. doi: 10.1002/2015GC006125
Davies, D. R., Wilson, C. R., & Kramer, S. C. (2011). Fluidity: A fully unstructured anisotropic adaptive mesh computational modeling framework for geodynamics. *Geochemistry, Geophysics, Geosystems*, *12*(6).
Di Giuseppe, E., van Hunen, J., Funiciello, F., Faccenna, C., & Giardini, D. (2008). Slab stiffness control of trench motion: Insights from numerical models. *Geochemistry, Geophysics, Geosystems*, *9*(2).
Espurt, N., Funiciello, F., Martinod, J., Guillaume, B., Regard, V., Faccenna, C., & Brusset, S. (2008). Flat subduction dynamics and deformation of the South American plate: Insights from analog modeling. *Tectonics*, *27*(3).
Faccenna, C., Becker, T. W., Lucente, F. P., Jolivet, L., & Rossetti, F. (2001). History of subduction and back arc extension in the Central Mediterranean. *Geophysical Journal International*, *145*(3), 809–820.
Forsyth, D., & Uyeda, S. (1975). On the relative importance of the driving forces of plate motion. *Geophysical Journal International*, *43*(1), 163–200.
Funiciello, F., Faccenna, C., Heuret, A., Lallemand, S., Di Giuseppe, E., & Becker, T. W. (2008). Trench migration, net rotation and slab–mantle coupling. *Earth and Planetary Science Letters*, *271*(1-4), 233–240.
Funiciello, F., Moroni, M., Piromallo, C., Faccenna, C., Cenedese, A., & Bui, H. A. (2006). Mapping mantle flow during retreating subduction: Laboratory models analyzed by feature tracking. *Journal of Geophysical Research: Solid Earth*, *111*(B3).
Garel, F., Goes, S., Davies, D. R., Davies, J. H., Kramer, S. C., & Wilson, C. R. (2014). Interaction of subducted slabs with the mantle transition-zone: A regime diagram from 2-D thermo-mechanical models with a mobile trench and an overriding plate. *Geochemistry, Geophysics, Geosystems*, *15*(5), 1739–1765.
Goes, S., Agrusta, R., van Hunen, J., & Garel, F. (2017). Subduction-transition zone interaction: A review. *Geosphere*, *13*(3), 644–664.
Goes, S., Capitanio, F. A., & Morra, G. (2008). Evidence of lower-mantle slab penetration phases in plate motions. *Nature*, *451*(7181), 981–984.
Goes, S., Capitanio, F. A., Morra, G., Seton, M., & Giardini, D. (2011). Signatures of downgoing plate-buoyancy driven subduction in Cenozoic plate motions. *Physics of the Earth and Planetary Interiors*, *184*(1-2), 1–13.
Gutscher, M. A., Malavieille, J., Lallemand, S., & Collot, J. Y. (1999). Tectonic segmentation of the North Andean margin: Impact of the Carnegie Ridge collision. *Earth and Planetary Science Letters*, *168*(3-4), 255–270.
Gutscher, M. A., Olivet, J. L., Aslanian, D., Eissen, J. P., & Maury, R. (1999). The

"lost Inca Plateau": Cause of flat subduction beneath Peru? *Earth and Planetary Science Letters*, *171*(3), 335–341.

Heuret, A., Funiciello, F., Faccenna, C., & Lallemand, S. (2007). Plate kinematics, slab shape and back-arc stress: A comparison between laboratory models and current subduction zones. *Earth and Planetary Science Letters*, *256*(3-4), 473–483.

Heuret, A., Lallemand, S., Funiciello, F., Piromallo, C., & Faccenna, C. (2011). Physical characteristics of subduction interface type seismogenic zones revisited. *Geochemistry, Geophysics, Geosystems*, *12*(1).

Holt, A. F., Becker, T. W., & Buffett, B. A. (2015). Trench migration and overriding plate stress in dynamic subduction models. *Geophysical Journal International*, *201*(1), 172–192.

Holt, A. F., Royden, L. H., & Becker, T. W. (2017). The dynamics of double slab subduction. *Geophysical Journal International*, *209*(1), 250–265.

Jarrard, R. D. (1986). Relations among subduction parameters. *Reviews of Geophysics*, *24*(2), 217–284.

Karato, S.-i., Riedel, M. R., & Yuen, D. A. (2001). Rheological structure and deformation of subducted slabs in the mantle transition zone: Implications for mantle circulation and deep earthquakes. *Physics of the Earth and Planetary Interiors*, *127*(1-4), 83–108.

Kearey, P., Klepeis, K. A., & Vine, F. J. (2009). *Global tectonics.* John Wiley & Sons.

Király, Á., Capitanio, F. A., Funiciello, F., & Faccenna, C. (2017). Subduction induced mantle flow: Length-scales and orientation of the toroidal cell. *Earth and Planetary Science Letters*, *479*, 284–297.

Kramer, S. C., Davies, D. R., & Wilson, C. R. (2021). Analytical solutions for mantle flow in cylindrical and spherical shells. *Geoscientific Model Development*, *14*(4), 1899–1919.

Kramer, S. C., Wilson, C. R., & Davies, D. R. (2012). An implicit free surface algorithm for geodynamical simulations. *Physics of the Earth and Planetary Interiors*, *194*, 25–37.

Lallemand, S., Heuret, A., & Boutelier, D. (2005). On the relationships between slab dip, back-arc stress, upper plate absolute motion, and crustal nature in subduction zones. *Geochemistry, Geophysics, Geosystems*, *6*(9).

Li, C., van der Hilst, R. D., Engdahl, E. R., & Burdick, S. (2008). A new global model for P wave speed variations in Earth's mantle. *Geochemistry, Geophysics, Geosystems*, *9*(5).

Lithgow-Bertelloni, C., & Richards, M. A. (1998). The dynamics of Cenozoic and Mesozoic plate motions. *Reviews of Geophysics*, *36*(1), 27–78.

Lonsdale, P. (2005). Creation of the Cocos and Nazca plates by fission of the Farallon plate. *Tectonophysics*, *404*(3-4), 237–264.

Mahadevan, L., Bendick, R., & Liang, H. (2010). Why subduction zones are curved. *Tectonics*, *29*(6).

Mann, P., & Taira, A. (2004). Global tectonic significance of the Solomon Islands and Ontong Java Plateau convergent zone. *Tectonophysics*, *389*(3-4), 137–190.

Martinod, J., Funiciello, F., Faccenna, C., Labanieh, S., & Regard, V. (2005). Dynamical effects of subducting ridges: insights from 3-D laboratory models. *Geophysical Journal International*, *163*(3), 1137–1150.

Mason, W. G., Moresi, L., Betts, P. G., & Miller, M. S. (2010). Three-dimensional numerical models of the influence of a buoyant oceanic plateau on subduction zones. *Tectonophysics*, *483*(1-2), 71–79.

Met Office. (2010 - 2015). Cartopy: a cartographic python library with a Matplotlib interface [Computer software manual]. Exeter, Devon. Retrieved from `https://scitools.org.uk/cartopy`

Morra, G., Chatelain, P., Tackley, P., & Koumoutsakos, P. (2007). Large scale three-

dimensional boundary element simulation of subduction. In *International conference on computational science* (pp. 1122–1129).
Morra, G., Chatelain, P., Tackley, P., & Koumoutsakos, P. (2009). Earth curvature effects on subduction morphology: Modeling subduction in a spherical setting. *Acta Geotechnica*, *4*(2), 95–105.
Morra, G., Quevedo, L., & Müller, R. D. (2012). Spherical dynamic models of top-down tectonics. *Geochemistry, Geophysics, Geosystems*, *13*(3).
Müller, R. D., Seton, M., Zahirovic, S., Williams, S. E., Matthews, K. J., Wright, N. M., ... Cannon, J. (2016). Ocean basin evolution and global-scale plate reorganization events since Pangea breakup. *Annual Review of Earth and Planetary Sciences*, *44*, 107–138.
Müller, R. D., Zahirovic, S., Williams, S. E., Cannon, J., Seton, M., Bower, D. J., ... Gurnis, M. (2019). A global plate model including lithospheric deformation along major rifts and orogens since the Triassic. *Tectonics*, *38*(6), 1884–1907.
Neal, C. R., Mahoney, J. J., Kroenke, L. W., Duncan, R. A., & Petterson, M. G. (1997). The Ontong Java Plateau. *Geophysical Monograph-American Geophysical Union*, *100*, 183–216.
OzBench, M., Regenauer-Lieb, K., Stegman, D. R., Morra, G., Farrington, R., Hale, A., ... Moresi, L. (2008). A model comparison study of large-scale mantle–lithosphere dynamics driven by subduction. *Physics of the Earth and Planetary Interiors*, *171*(1-4), 224–234.
Pelletier, B., Calmant, S., & Pillet, R. (1998). Current tectonics of the Tonga–New Hebrides region. *Earth and Planetary Science Letters*, *164*(1-2), 263–276.
Pozrikidis, C. (1992). *Boundary integral and singularity methods for linearized viscous flow.* Cambridge university press.
Ribe, N. M. (2010). Bending mechanics and mode selection in free subduction: A thin-sheet analysis. *Geophysical Journal International*, *180*(2), 559–576.
Schellart, W. P. (2004). Kinematics of subduction and subduction-induced flow in the upper mantle. *Journal of Geophysical Research: Solid Earth*, *109*(B7).
Schellart, W. P. (2008). Kinematics and flow patterns in deep mantle and upper mantle subduction models: Influence of the mantle depth and slab to mantle viscosity ratio. *Geochemistry, Geophysics, Geosystems*, *9*(3).
Schellart, W. P., Freeman, J., Stegman, D. R., Moresi, L., & May, D. (2007). Evolution and diversity of subduction zones controlled by slab width. *Nature*, *446*(7133), 308–311.
Schepers, G., van Hinsbergen, D. J., Spakman, W., Kosters, M. E., Boschman, L. M., & McQuarrie, N. (2017). South-American plate advance and forced Andean trench retreat as drivers for transient flat subduction episodes. *Nature communications*, *8*(1), 1–9.
Scholl, D. W., Buffington, E. C., & Marlow, M. S. (1975). Plate tectonics and the structural evolution of the Aleutian–Bering Sea region. *Geological Society of America Special Papers*, *151*, 1–32.
Sdrolias, M., & Müller, R. D. (2006). Controls on back-arc basin formation. *Geochemistry, Geophysics, Geosystems*, *7*(4).
Sharples, W., Jadamec, M. A., Moresi, L.-N., & Capitanio, F. A. (2014). Overriding plate controls on subduction evolution. *Journal of Geophysical Research: Solid Earth*, *119*(8), 6684–6704.
Stegman, D. R., Farrington, R., Capitanio, F. A., & Schellart, W. P. (2010). A regime diagram for subduction styles from 3-D numerical models of free subduction. *Tectonophysics*, *483*(1-2), 29–45.
Stegman, D. R., Freeman, J., Schellart, W. P., Moresi, L., & May, D. (2006). Influence of trench width on subduction hinge retreat rates in 3-D models of slab rollback. *Geochemistry, Geophysics, Geosystems*, *7*(3).
Stegman, D. R., Schellart, W. P., & Freeman, J. (2010). Competing influences of plate width and far-field boundary conditions on trench migration and mor-

phology of subducted slabs in the upper mantle. *Tectonophysics*, *483*(1-2), 46–57.

Stern, R. J. (2002). Subduction zones. *Reviews of geophysics*, *40*(4), 3–1.

Stotz, I. L., Iaffaldano, G., & Davies, D. R. (2017). Late Miocene Pacific plate kinematic change explained with coupled global models of mantle and lithosphere dynamics. *Geophysical Research Letters*, *44*(14), 7177–7186.

Strak, V., & Schellart, W. P. (2016). Control of slab width on subduction-induced upper mantle flow and associated upwellings: Insights from analog models. *Journal of Geophysical Research: Solid Earth*, *121*(6), 4641–4654.

Tagawa, M., Nakakuki, T., & Tajima, F. (2007). Dynamical modeling of trench retreat driven by the slab interaction with the mantle transition zone. *Earth, planets and space*, *59*(2), 65–74.

Torii, Y., & Yoshioka, S. (2007). Physical conditions producing slab stagnation: Constraints of the Clapeyron slope, mantle viscosity, trench retreat, and dip angles. *Tectonophysics*, *445*(3-4), 200–209.

van der Hilst, R., & Seno, T. (1993). Effects of relative plate motion on the deep structure and penetration depth of slabs below the Izu-Bonin and Mariana island arcs. *Earth and Planetary Science Letters*, *120*(3-4), 395–407.

van der Meer, D. G., van Hinsbergen, D. J., & Spakman, W. (2018). Atlas of the underworld: Slab remnants in the mantle, their sinking history, and a new outlook on lower mantle viscosity. *Tectonophysics*, *723*, 309–448.

van Dinther, Y., Morra, G., Funiciello, F., & Faccenna, C. (2010). Role of the overriding plate in the subduction process: Insights from numerical models. *Tectonophysics*, *484*(1-4), 74–86.

van Hunen, J., van den Berg, A. P., & Vlaar, N. J. (2002). On the role of subducting oceanic plateaus in the development of shallow flat subduction. *Tectonophysics*, *352*(3-4), 317–333.

Wheeler, P., & White, N. (2002). Measuring dynamic topography: An analysis of Southeast Asia. *Tectonics*, *21*(5), 4–1.

Whittaker, J. M., Müller, R. D., Sdrolias, M., & Heine, C. (2007). Sunda-Java trench kinematics, slab window formation and overriding plate deformation since the Cretaceous. *Earth and Planetary Science Letters*, *255*(3-4), 445–457.

Wilson, C. R. (2009). *Modelling multiple-material flows on adaptive unstructured meshes.* PhD Thesis, Imperial College London, UK.

Supporting Information: 'How sphericity combines with the age and width of slabs to dictate the dynamics and evolution of subduction systems on Earth'

Fangqin Chen[1], D. Rhodri Davies[1], Saskia Goes[2], Lior Suchoy[2], Stephan C. Kramer[2]

[1]Research School of Earth Sciences, The Australian National University, Canberra, ACT, Australia

[2]Department of Earth Science and Engineering, Imperial College London, London, UK

Contents of this file

1. Figures S1 to S3

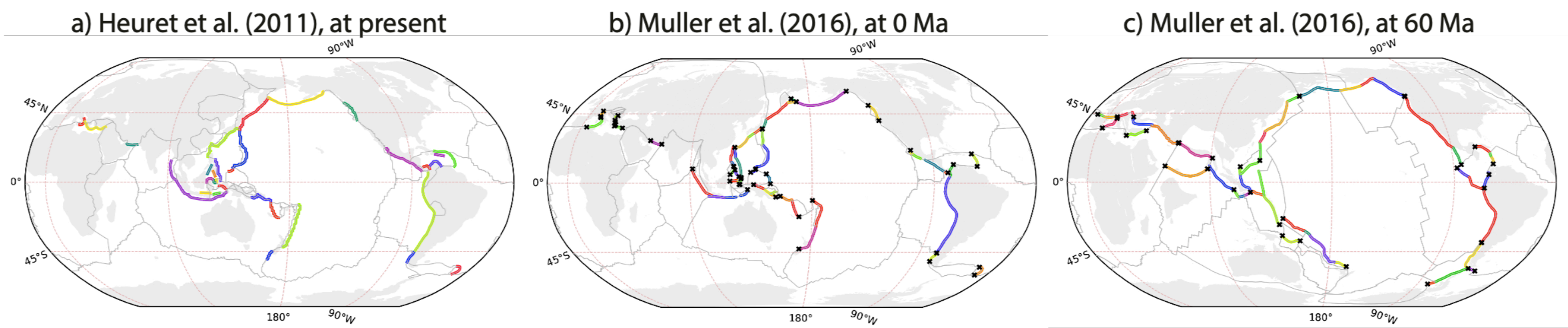

Figure S1. (a) Map of subduction zones from Heuret et al. (2011). (b) and (c) Map of trench segments based on plate reconstruction at present and at 60 Myr by Müller et al. (2016). In (b) and (c), black crosses represent edges of subduction zones. Trench segments within each subduction zones were merged when calculating trench length.

References

Heuret, A., Lallemand, S., Funiciello, F., Piromallo, C., & Faccenna, C. (2011). Physical characteristics of subduction interface type seismogenic zones revisited. *Geochemistry, Geophysics, Geosystems*, *12*(1).

Müller, R. D., Seton, M., Zahirovic, S., Williams, S. E., Matthews, K. J., Wright, N. M., ... Cannon, J. (2016). Ocean basin evolution and global-scale plate reorganization events since Pangea breakup. *Annual Review of Earth and Planetary Sciences*, *44*, 107–138.

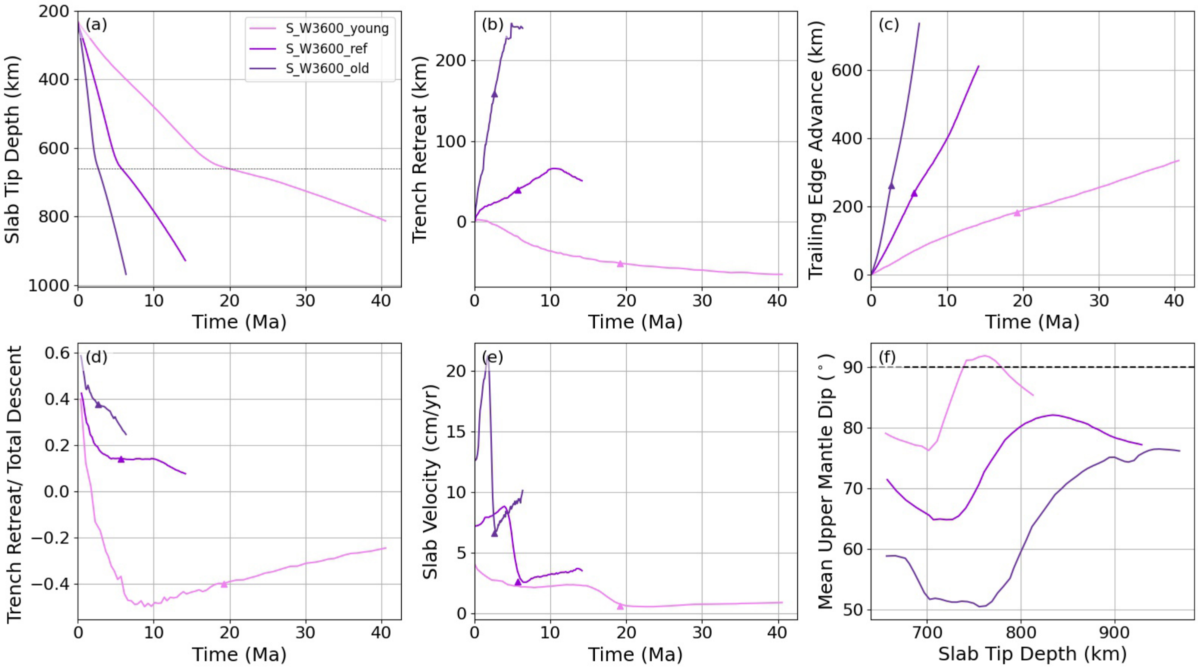

Figure S2. Comparison between spherical simulations with a plate width of 3600 km: (a) slab tip depth, as a function of time, where the upper–lower mantle boundary is indicated by the black dotted line at 660 km depth; (b) amount of trench retreat; (c) amount of plate advance, measured at the plate's trailing edge; (d) ratio of trench retreat to total descent, which is the sum of trench retreat and trailing edge advance; (e) slab sinking velocity; and (f) average slab dip in the upper mantle, with the black dashed line indicating a vertical slab with dip angle of 90°. Triangles indicate the time of slab tip transition-zone interaction. All measurements are taken at the symmetry plane.

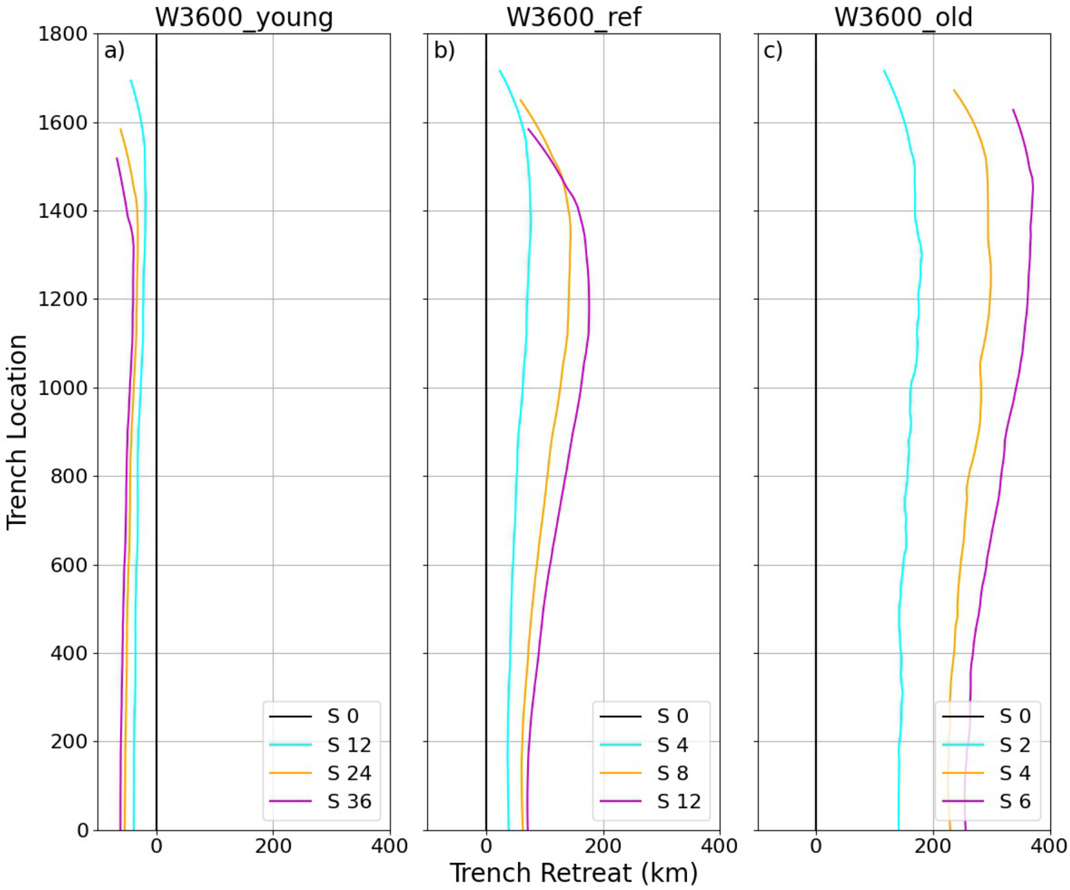

Figure S3. Spatio-temporal evolution of trench location in spherical (S) simulations, at a plate width of 3600 km. Times given in Myr since simulation initiation. (a) $H = 45$ km, $\Delta\rho = 40\,\mathrm{kg\,m^{-3}}$; (b) $H = 70$ km, $\Delta\rho = 80\,\mathrm{kg\,m^{-3}}$; (c) $H = 100$ km, $\Delta\rho = 120\,\mathrm{kg\,m^{-3}}$.